MOLECULAR DYNAMICS SIMULATIONS OF ION–SURFACE INTERACTIONS WITH APPLICATIONS TO PLASMA PROCESSING

David B. Graves and Cameron F. Abrams

Department of Chemical Engineering, University of California–Berkeley, Berkeley, California 94720

I. Introduction

A. Plasma Processing

The topic of this article is the use of molecular dynamics (MD) simulations of positive ion–surface interactions for insights into the chemical and physical processes that occur at surfaces immersed in glow discharge plasmas. To understand the significance of this topic, it is necessary to have some background in the technology and its major industrial application (Lieberman and Lichtenberg, 1994). The term "plasma" in this context refers

ADVANCES IN CHEMICAL ENGINEERING, VOL. 28 0065-2377/01 $35.00

to an ionized gas. Irving Langmuir is generally credited with first using the term to refer to ionized gases. The study of the physics of ionized gases has received a great deal of attention since then (Chen, 1984). Plasma physics is indeed a large and well-established field, but it generally deals with the fully ionized, usually very hot and magnetized plasmas that occur in stellar environments or in thermonuclear fusion. Fully ionized, magnetized plasmas are subject to many instabilites, and turbulence is often important. The focus of much of plasma physics research is on creating and stabilizing very hot, fully ionized plasmas. Controlled thermonuclear fusion for power generation has been limited by the difficulties in confining the plasma at sufficiently high temperatures for a sufficient length of time. The types of plasmas used for the semiconductor materials processing applications are quite different from the plasmas commonly associated with the term "plasma physics." It should be noted, however, that when the plasmas used for fusion interact with confining walls, some of the same considerations that can dominate semiconductor processing are present (Post and Behrish, 1986). Compared to plasma physics, the field of plasma materials processing has generally received much less attention, at least in terms of the fundamental science.

In plasma processing of semiconductors, the plasmas are usually highly nonequilibrium, and the gas is only weakly to partially ionized. It is understood, of course, that the term "semiconductor" refers not only to semiconducting materials but also to the conductors and dielectrics used in semiconductor devices. The term "nonequilibrium" here means that the charged species (electrons and ions) generally have a much higher average kinetic energy than the neutral species. A partially ionized gas is a mixture of neutral and charged species. The plasmas are usually created by application of electric and magnetic fields to a relatively low-pressure gas. In most cases, the gas pressure is between a few millitorrs and several torrs. The fields can range from dc to microwave frequencies. Under the right conditions the neutral, mostly insulating gas can be "broken down" and becomes conductive—due mainly to the creation of a sufficient concentration of free electrons in the gas. By passing currents through the gas, the charged species are heated, thereby sustaining the plasma. The peak neutral gas temperature can vary from near room temperature to over 2000 K. The average electron kinetic energy can approach 10 eV/electron (equivalently, over 100,000 K), and positive ions near the boundary of the plasma can reach energies of the same order. Ions accelerated by the relatively large electric fields in the electrical boundary layer of the plasma (i.e., the "sheath") can reach an energy as high as the applied voltage before impacting the surface. Typical conditions in plasma processing are listed in Table I. The reason for the big difference between neutral and charged species energies is that charged species are lost to walls faster than they are able to transfer to neutrals via collisions the energy

TABLE I
TYPICAL CONDITIONS IN NONEQUILIBRIUM PLASMAS

Gas pressure	1–1000 mTorr
Gas temperature	300–2000 K (0.03–0.15 eV/atom)
Degree of ionization ($N_{plasma}/N_{neutral}$)	10^{-6}–10^{-2}
Average electron energy	1–10 eV
Average ion energy in plasma	0.05–1 eV
Average ion energy impacting surface	10–1000 eV
Typical plasma dimension	0.1–1 m

they receive from the applied fields. At higher neutral gas pressures, this is no longer the case, and the neutral gas can become quite hot. A common example is arc welding.

Plasma processing of semiconductors relies on a combination of chemical and physical processes at surfaces exposed to the plasma. Figure 1 is a sketch of a typical plasma chamber used for processing the surface of a silicon wafer. In the example in Fig. 1, the plasma is excited using an external "stovetop" coil, powered using a radiofrequency current (RF1). Since the RF current in the external coil induces a current in the plasma, the power coupling is "inductive." The wafer has a separate, capacitive RF power applied to it (RF2), which allows independent control of ion energy impacting the surface.

Wafers are usually processed one at a time in the chamber. Gas flows into the chamber and is pumped into the exhaust. External power is applied electrically and the plasma is generated and sustained. The plasma modifies the surface of the wafer in two basic ways. First, the inlet gases are dissociated via electron-impact molecular dissociation into reactive free radicals

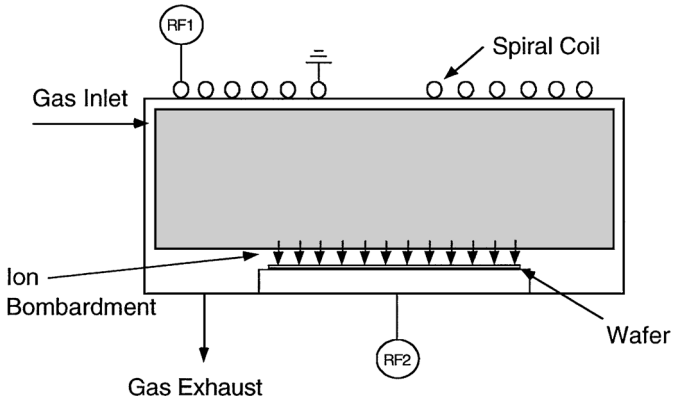

FIG. 1. Schematic diagram of a typical plasma reactor used to etch patterns on wafers.

(e.g., F, CF, CF_2, from CF_4). These radicals generally adsorb at all surfaces within the chamber, including the wafer. In addition, energetic positive ions, accelerated by the strong electric fields at the boundary of the plasma, impact surfaces. The combination of adsorbed radicals and ion impact promotes surface chemical reaction at low temperatures. Relatively low surface temperatures are a major advantage of plasma processes when processing temperature-sensitive microelectronic devices. Material can be removed, in which case the plasma etches the surface, or material can be deposited, in which case the plasma deposits a thin film. In some cases, plasmas are used to simply modify the surface functional groups or remove surface debris. Plasmas are commonly used for all of these applications in semiconductor manufacturing.

B. Length Scales in Plasma Processing

A proper understanding of plasma processing and semiconductor device manufacturing requires a consideration of the range of length scales involved. Semiconductor products such as microprocessors or memory chips are discrete devices and are manufactured on silicon wafers. Each wafer is processed to make a set of nominally identical chips, or "die." The diameter of the wafer for leading edge semiconductor factories, or fabs, has steadily increased, from 50 mm in 1970 to 300 mm in 2001. The "wafer scale" determines the size of the equipment, typically of the order of a meter. However, there are several other natural length scales: the scale of the chip or die ($\sim$1 cm), the scale of the critical dimensions within the device ($\sim$0.1 μm), and the scale of the dimensions that can affect device properties ($\sim$1 Å). The chip scale is important since the transistors must be nominally identical across the entire chip. The other two scales affect the behavior of an individual transistor. As in many other areas of chemical processing, treating multiple length scales can be challenging.

Chips are generally made up of sets of interconnected solid state transistors, or switches. The solid-state transistors, most commonly metal–oxide–semiconductor field effect transistors (MOSFETs), consist of source, gate, and drain. In manufacturing these devices, a complex set of processes is used, involving lithographic pattern transfer, implantation, diffusion, thin-film growth, deposition, polishing, etching, and surface cleaning. Over 300 individual steps are typically used in current leading edge device manufacturing processes (Wolf and Tauber, 2000). The characteristic dimensions of these features are now of the order of 100 nm or 0.1 μm. In etching, one must ensure that features are controlled to within this dimensional constraint. For example, the current nominal width of the gate electrode for a MOSFET is

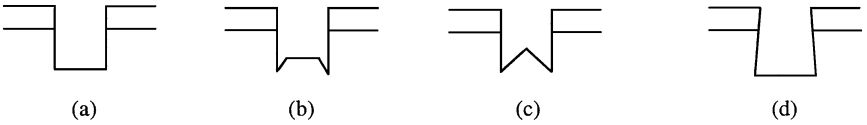

FIG. 2. Examples of several etch profiles: (a) near-straight wall; (b) microtrenches; (c) broad microtrenches; (d) reentrant shape.

about 200 nm, but this width must be controlled to within about ± 10 nm. Control of dimensions on the feature length scale is one of the most important tasks faced by equipment and process engineers.

During plasma etching (or deposition in some cases), ion–surface interactions strongly affect the shape evolution of features—indeed, this is why the technology is used. There are examples (circa 2000) of the use of plasma etching to etch features with lateral dimensions of the order of 10 nm. Etch anisotropy (i.e., etching in one preferred direction) and etch selectivity (etching only one material) are important attributes. As noted above, it has proven possible to etch very small features indeed if the mask can be defined—this has been part of the reason that lithography has been and will probably continue to be viewed as the major limiting factor in future developments. However, the plasma etch step can introduce many shape artifacts, the mechanisms for which are imperfectly understood. Other known or suspected effects include feature sidewall charging deflecting ion trajectories, electrical currents from the plasma causing electrical damage to nascent devices, and stress localization in features promoting or retarding etching. Figure 2 shows sketches of some common etch profile shapes. As features shrink and as demands on device performance increase, processing technologies are under increasing pressure to achieve compositional and structural control over atomic dimensions. The consequence is that plasma processes must be understood and controlled sufficiently well that near-atomic dimensional control can be achieved over macroscopic length scales. The ratio of the smallest controlled length scale ($\sim$1 Å) to the wafer size ($\sim$300–400 mm) will then approach 9 to 10 orders of magnitude.

C. The Nature of Plasma–Surface Interactions

One of the most important aspects of plasma–surface processing is that *the plasma itself often strongly modifies the near-surface region*. An example of this is shown schematically in Figs. 3a and b, in the case of etching. Figure 3a is a depth profile of an originally crystalline silicon surface that has been exposed to a chlorine plasma. (Chlorine plasma is commonly used to etch silicon and other materials.) The plasma has created various silicon

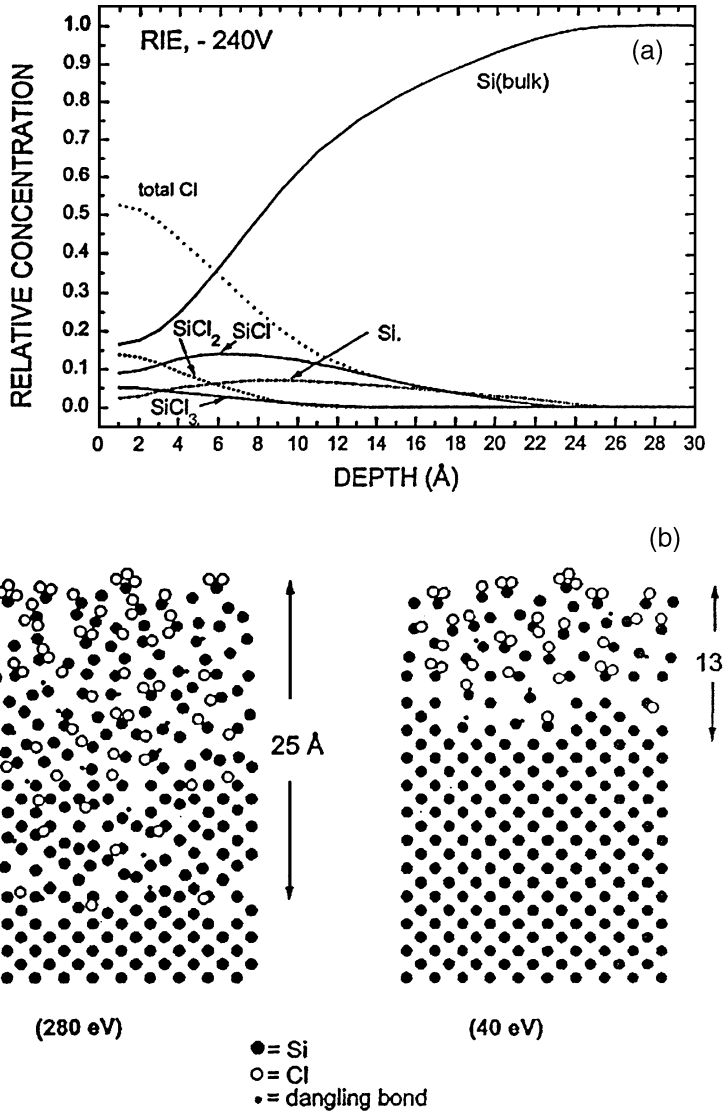

FIG. 3. (a) Steady-state depth composition profile of an originally crystalline silicon surface that has been exposed to a chlorine plasma, obtained from angle-resolved X-ray photoelectron spectroscopy. (b) Corresponding side-view schematics of near-surface atomic coordination: left, 280-eV ions; right, 40-eV ions. (From Layadi *et al.,* 1997.)

chloride products, as well as Si dangling bonds, to a depth of about 30 Å. The depth profile was obtained by angle-resolved X-ray photoelectron spectroscopy. Figure 3b is a sketch at the atomistic level of the near-surface region as envisioned by the authors (Layadi *et al.,* 1997). For the purposes of this discussion, the most important aspect to note is that the plasma has strongly altered the chemical and physical characteristics of the near-surface region (several nanometers). Similar arguments apply to plasma deposition of thin films, as well. Any fundamental understanding of plasma–surface chemistry must come to grips with the profound changes induced at surfaces by the plasma. This complicates studies of plasma–surface chemistry since every time the plasma environment changes, the surface changes. The surface chemistry in general also changes. It is argued that this fundamental fact renders plasma–surface chemistry unusually difficult, and it has a correspondingly complicating effect on simulations of reactive ion–surface interactions.

D. Ion–Surface Interactions in Plasma Processing

The topic of this article is the use of MD to simulate the effects of energetic, often reactive and molecular, positive ions on surfaces exposed to plasmas. Positive ions naturally impact surfaces that form their boundaries since, for the most part, all positive ions created within the plasma are lost to walls rather than to volume recombination with electrons or negative ions (Lieberman and Lichtenberg, 1994). Thin boundary layers called "sheaths" form at walls, retarding electron motion out of the plasma and accelerating positive ions. It is often the case that the final acceleration across the sheath results in few or essentially no ion-neutral collisions, with the result that ions impact surfaces with energies of the order of hundreds to even thousands of volts, depending on the magnitude of externally applied surface voltages.

Chemical bonds are typically of the order of several electron volts, so it is obvious that ions from plasmas can dramatically affect surface chemistry. In its simplest manifestation, unreactive (e.g., Ar^+) ions impact surfaces, resulting in sputtering, or the physical removal of surface atoms by a process analogous to "sandblasting." Sputtering is a very common technique to deposit thin films: material sputtered from one surface will generally condense to form a thin film on another surface. Virtually any material can be sputtered, and sputter deposition has been widely exploited in a variety of applications, including microelectronics manufacturing, optical films, corrosion resistance, and antireflection coatings and for films for decorative purposes. More commonly, ion–surface interactions occur within plasmas that contain chemically reactive species. Plasmas can be used for chemical

vapor deposition, for etching or removal of material, or for cleaning or surface modification. In all cases, ion–surface interactions clearly play a role, and often this is a crucially important role.

One motivation for MD studies of ion–surface interactions is to develop a systematic understanding of plasma–surface interactions. Reactive free radicals created in the plasma, as detailed very ably in the article in this volume on SiH_x radical–surface chemistry by Maroudas and co-workers, are one important part of the chemistry induced by plasmas at surfaces being processed. However, the energy deposited by ions, and often the associated directionality of those ions when they interact with surface microfeatures, usually plays the most dramatic role. The ion flux in all applications of interest here is relatively small, and the time and length scales associated with a single ion impact are sufficiently short and small, respectively, that ion impacts do not overlap in time. It happens, fortuitously, that a single ion impact under conditions most commonly relevant to plasma–surface interactions can be treated with a collection of atoms numbering no more than several thousand, on a time scale usually less than 5 ps. In some cases, a few hundred atoms followed for 1 ps or less is sufficient. With semiempirical interatomic potentials, this means that thousands of impacts can be simulated on personal computers (circa 2000) in reasonable times. The combination of increasingly inexpensive computing, the development of reasonably accurate interatomic potentials for some materials of common interest in semiconductor manufacturing, and the fact that plasma processing mainly involves the cumulative effects of individual ion impacts has made technologically relevant studies of reactive ion–surface interaction feasible at a modest cost.

II. Use of Molecular Dynamics to Study Ion–Surface Interactions

A. Simulation Procedure

In plasma processing, singly charged positive ions impact surfaces at energies between about 5 and 1000 eV. A variety of chemical and physical events occur that dramatically affect surface chemistry. The basic procedure in simulating this process is summarized in this section. Details can be found elsewhere (Barone, 1995; Helmer, 1998; Abrams, 2000). It should be noted that studies of ion sputtering of surfaces using classical trajectory simulations date back to the late 1960s and the pioneering efforts of Harrison (Harrison *et al.,* 1968, 1978; Harrison, 1988; Smith *et al.,* 1989, 1990). Although some of the early studies did not use periodic boundary conditions and they focused on relatively simple physical sputtering, many of the basic ideas for reactive

ion–surface trajectory simulations were developed at this time. Garrison and co-workers extensively studied physical sputtering of silicon and various metals by rare-gas ions (Galijatovic *et al.,* 1996; Garrison *et al.,* 1987). Many other authors have also used MD to study sputtering processes (Urbassek, 1997; Coronell *et al.,* 1998; Kress *et al.,* 1999). More recent efforts to use MD to study energetic species–surface interactions include etching and other plasma–surface processing studies (Feil *et al.,* 1993; Barone and Graves, 1995a,b, 1996; Athavale and Economou, 1995; Hanson *et al.,* 1997, 1998; Helmer and Graves, 1997, 1998; Kubota *et al.,* 1998; Abrams and Graves, 1998, 1999, 2000a–d; Wijesundara *et al.,* 2000).

Ion–surface interactions are simulated by launching an energetic ion at a surface consisting of a few hundred to a few thousand atoms, as illustrated in Fig. 4 . A collection of several hundred to several thousand atoms, referred to as the "cell" or "surface layer," represents the semiinfinite surface. A sketch of a copper surface is shown in Fig. 4. The lateral boundaries are periodic to simulate the semiinfinite surface with as small a set of atoms as possible, and the bottom two layers are fixed in space to anchor the cell. The "ion" is initially placed outside the range of interaction with the surface and is then launched with the desired energy, angle of impact, and impact location on the surface and allowed to interact with the surface atoms. The "collision cascade" occurs as the ion impacts the surface and transfers kinetic energy to the atoms in the cell. Some surface atoms may fly off the surface (termed "sputtering"), and others may move on the surface of the cell or to some other position within the cell. The snapshot in Fig. 4 at 1 ps illustrates sputtered atoms leaving the surface. The ion may reflect or imbed in the cell. One is generally interested in simulating the effects of many ions over surfaces

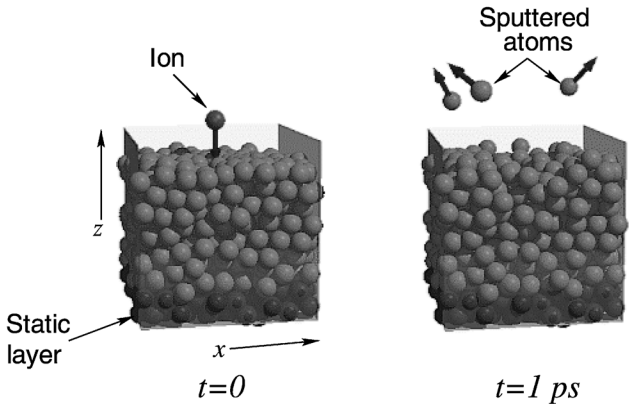

FIG. 4. Side view of a simulated copper layer undergoing Cu^+ ion bombardment and sputtering at time 0 (left) and after 1 ps has elapsed (right). (From Abrams, 2000.)

of macroscopic dimensions, so to obtain statistically significant results, ion impact points are selected at random and tens to hundreds of impacts are simulated. In some cases, the surface is allowed to change after each impact, and in other cases, it is more appropriate to use the same initial conditions for each trajectory. If the proper set of interatomic potentials is used, chemical bond breaking and formation can be simulated.

The system is described using classical mechanics. Each atom is treated separately with interatomic potentials describing the interactions between atoms, including bonding interactions. The interatomic potential is described as $U = U(\{\mathbf{r_i}\})$, in which each atom's position is represented as the vector $\mathbf{r_i}$, and the scalar potential U includes all interatomic interactions. By taking the gradient of the potential with respect to position, $\partial U/\partial \mathbf{r_i} = -m_i \partial^2 \mathbf{r_i}/\partial t^2$, one obtains the set of N coupled equations of motion of the N atoms. The system is simulated by numerically solving the coupled equations of motion of all atoms, as described in MD texts (Allen and Tildsley, 1987; Haile, 1992; Rappaport, 1995). Tully (1980) addresses the adequacy of a classical description in studies of gas–surface interactions and concludes that for atoms heavier than C, quantum effects such as tunneling can be ignored. Rappaport (1995) points out the practical fact that MD simulations have been successful, sometimes surprisingly so, in predicting phenomena that can be measured. The main issue in MD simulations is the accuracy of the interatomic potentials. Some function describing the potential energy as a function of relative atomic distances must be developed. This function must be capable of reproducing all of the important interactions between atoms including bond breaking and forming.

One approach would be to describe electrons via quantum mechanics and the Born–Oppenheimer approximation, assuming that nuclear motion is decoupled from electron dynamics and can be described classically. At each point in time, the total system wavefunction is computed, resulting in the potential energy surface U. From this, the instantaneous forces on all nuclei can be computed from the gradient, and the nuclear positions and velocities can be advanced. Obviously appealing in its rigor, this approach is completely impractical at present for studies of reactive ion–surface interactions. As discussed in Section III, it is necessary to simulate several thousand trajectories for of the order of hundreds to thousands of atoms to obtain results for a single set of conditions (ion type, ion energy, surface materials, etc.). Further, in the MD simulations used for ion–surface simulations, it is assumed that the "ion" is in fact a fast neutral. In part, this assumption is made because we believe that for most systems of interest, the ion recombines via the emission of an Auger electron within a few angstroms of the surface (Helmer, 1998). However, this assumption is necessary because potential energy surfaces are not generally available for charged species.

In addition to assuming that the "ion" is a fast neutral (although the term "ion" will continue to be used to describe the energetic species impacting the surface from the plasma), we neglect any but the ground electronic state. In particular, as Helmer (1998) points out, the recombination process may well result in an excited molecular species that can dissociate before impacting the surface. Reflected species could pick up an electron as it leaves the surface. And image forces in the surface can deflect the motion of charged species near the surface. The procedure described here has neglected all of these potential effects, and we rely on the fact that for kinetic energies above a few electron volts, the ion–surface interaction process is dominated by the kinetic energy exchanged upon impact. There will no doubt be systems for which these approximations will not be adequate, but we must leave their consideration to future work.

Maroudas and co-workers have described a hierarchical scheme for atomistic simulations involving the use of electronic structure calculations to develop and test semiempirical potentials that are in turn used for MD simulations. These results can sometimes be used to develop elementary step transition probabilities for use in dynamic Monte Carlo schemes. With Monte Carlo techniques, the well-known length and time scale limitations of MD can be greatly extended. This hierarchical approach appears to have great promise for the development of simulation strategies that will allow studies of a wide range of practical surface and thin-film chemical and physical processes.

For the purposes of the present article, rather than list the mathematical forms for the interatomic potentials used in the results that follow, we simply cite the original references. The interested reader can consult these papers and the references cited therein for more detailed information. Barone and Graves (1995a,b) and Barone (1995) used three-body Stillinger–Weber (1989) potentials for Si–Si, F–F, and Si–F interactions. Ar was treated with repulsive Moliere pair potentials. Helmer and Graves (1997, 1998) and Helmer (1998) also used the potentials developed by Feil *et al.* (1993) for Si–Cl and Cl–Cl interactions, by adjusting parameter values in the associated Stillinger–Weber potentials. Abrams and Graves (1998, 1999, 2000a–d) and Abrams (2000) used the potentials developed by Tanaka *et al.* (2000) for C–F, C–C, and F–F interactions, based on the ideas of Brenner (1990, 1992) and Tersoff (1988, 1989). Abrams introduced potentials for the Si-C-F system, using the Tanaka *et al.* (2000) formalism and, also, using results from Beardmore and Smith (1996).

The surface layer in Fig. 4 will be heated as a result of the energetic ion impact, since the lateral boundaries are periodic and the bottom layers are fixed. The kinetic energy transferred from the impinging ion to the surface will also result in bonds broken, movement of atoms on and within the layer,

sputtering, and so on. Unless some means to remove the energy from the layer is incorporated into the simulation, the layer temperature will rise. In contrast, for the real case of an ion impacting an essentially semiinfinite surface, the local "temperature" near the impact point will rise, then decrease as the energy is dissipated to the surface. Neither the *NVE* (constant number, volume, and energy) nor the *NVT* (constant temperature) cases is entirely appropriate. Various means have been employed to deal with this problem by different investigators (see, e.g., Barone, 1995). It would seem that the most realistic way to deal with this is to use a simulation cell sufficiently large and an ion energy sufficiently low that the simulated system approaches the actual case of a semiinfinite layer that can dissipate the ion impact kinetic energy without heating. This avoids the difficulty of trying to simulate the dynamic process of energy transfer in a finite cell either with boundary layers that remove heat or through a scheme to rescale all atomic velocities throughout the cell based on some arbitrary algorithm.

Obviously, the size of the cell, both laterally and in depth, is a crucially important factor with respect to possible artifacts related to the finite system size. In addition, since the simulation time scales approximately as the cube of the number of atoms in the cell, it is important to establish just how large the system must be to avoid artifacts. The best procedure seems to be the most straightforward—increase the cell size until the results stop changing significantly. Since results must be collected and analyzed statistically, this can be time-consuming, but there is no alternative that avoids arbitrary schemes. Similar comments apply to the choice of time taken per trajectory simulation. In some cases, such as sputtering (or ion scattering), when the sputtered (scattered) species leaves the surface within a few tenths of a picosecond or less (Harrison, 1988), one needs very short integration times. However, if chemistry is important, several picoseconds or more may be needed for the reactions to occur. Of course, there will also be processes that will occur on much longer time scales due to normal thermally induced diffusion and reaction processes, but these must be dealt with using other approaches, in general.

Another important question relates to how to simulate the relatively long times between ion impacts. If one brings an ion into the layer, follows the collision cascade trajectory for several picoseconds, then cools the layer to room temperature and, finally, allows another ion to impact the layer, does this not increase the ion flux by many orders of magnitude above that observed experimentally? In fact, we argue that another interpretation of the simulation scheme is more appropriate. After the layer is cooled to 300 K, by bringing another ion into the layer immediately, we are in effect assuming that nothing happens to the layer between the time the layer has cooled and the time another ion hits. Clearly, this is an approximation, since the layer will relax, and diffusion and some reaction may occur to some extent during

the milliseconds to seconds between impacts. However, the main processes in most cases occur during the brief but intense times following ion impact, and by incorporating the cumulative effects of the ion impacts, we expect that most of the important processes have been included. Future work will include adding, for example, Monte Carlo methods to treat more rigorously the relatively infrequent events between ion impacts.

III. Mechanisms of Ion-Assisted Etching

A. Experimental Studies of Ion-Assisted Etching Mechanisms

The mechanisms of plasma or ion-assisted etching have long been a subject of interest and even controversy. It has been known since the classic experiment of Coburn and Winters (1979) that plasma etching is usually the synergistic result of the combination of ion bombardment and neutral chemical reaction. The best-known example is silicon etching by fluorine and argon ions. In a vacuum beam system, the etch rate of a silicon film on a quartz crystal microbalance is measured vs. time. A beam of XeF_2 supplies the F atoms since XeF_2 decomposes readily at the surface. At first, only the XeF_2 beam hits the silicon, and at room temperature a small but measurable etch rate is observed. However, when the Ar^+ beam (e.g., 450 eV) is added, the etch rate jumps dramatically. Finally, when only the ion beam hits the surface, one observes the relatively low physical sputtering rate. This effect is referred to as the "ion-neutral synergism," but the basic idea is simple: the ion beam supplies the energy for F to etch Si to form the thermodynamically favored product, SiF_4. The room-temperature surface is evidently insufficient to scale the activation energy barrier. This simple fact, coupled with the naturally directional nature of ion flux to the surface—recall that ions are accelerated perpendicular to the surface by the natural and applied electric fields at surfaces—results in the characteristically anisotropic etching pattern that is so important in semiconductor manufacturing. Indeed, ion-assisted etching is capable of remarkable degrees of pattern transfer fidelity, as noted above.

Arguments about mechanisms all recognize that etching must consist of several steps occurring in series: adsorption of etchant, then creation of etch product, followed by desorption of the etch product. What are the respective roles of neutral and ions? The most common explanation is that the neutral etchant (the F atoms in the case above) penetrates the top few atomic layers of the silicon, breaking Si–Si bonds in the process. The insertion of F into the near-surface silicon lattice is then thought to weaken this layer so as to make it easier for the bombarding ions to sputter the top surface region. In

this scenario, ions play the role of promoting the third step in the etching sequence: product desorption. We term this mechanism "chemically assisted physical sputtering." Another mechanism that had been proposed is that ion bombardment, by damaging the near-surface region, creates additional adsorption sites for F atoms, which results in greater sputtering and etching. In this case, ions play the role of increasing the rate of the first step, as well as the third step. We call this "damage-enhanced etching." A third mechanism is that ion bombardment greatly increases the rate of creation of etch products and that these products desorb thermally, long after the ion impact. This mechanism envisions ion enhancement of the middle step: formation of the etch product. We call this mechanism "chemical etching."

Experimental studies of etch mechanisms tend to be indirect: the ion interacts with the surface over length scales of tens to hundreds of angstroms and time scales of the order of 10^{-12} s. Direct observation is therefore quite difficult. A detailed discussion of the surface science aspects of etching was presented by Winters and Coburn (1992). The experimental evidence relied primarily on the energy distribution of products and on the delay of surface emission of products following ion bombardment. If products were mainly physically sputtered, they should follow the energy distribution for sputtered products that had been established both experimentally and theoretically (Sigmund, 1969). In addition, sputtered products leave the surface on the time scale of the energy deposition: about 10^{-12} s. If products were chemically sputtered, they should leaves the surface thermalized at the surface temperature. The damage-enhanced etching model was easily disproved (at least for Si etched with F) by Winters and Coburn (1992) by simply preexposing a silicon film on a quartz microbalance to Ar^+, then seeing if subsequent F uptake was increased compared to that with no preexposure to the ion beam. No effect was observed so this mechanism was rejected for Si etching by F. However, these authors point out that for W, the effects of ion preexposure can be dramatic in enhancing the halogen uptake.

Evidence has been presented for both chemically assisted physical sputtering and chemical sputtering from the energy distributions of products and the time dependence of their desorption. Figure 5 is a plot of measured etch product flux versus energy (Oostra *et al.,* 1986). SiF_3^+ measured in a mass spectrometer reflects evolved SiF_4 from the surface etched with SF_6 and 3-keV Ar^+. At 50 K, the surface is sufficiently cold that only physically sputtered products emerge, and the characteristic "cascade" energy distribution is seen. The cascade energy distribution for flux vs. energy follows the following relation

$$f_{cc} = \frac{K_{cc} 2U_0 E}{(U_0 + E)^3},$$

where f_{cc} is the fractional probability density distribution $(\text{eV m}^2\,\text{s})^{-1}$, K_{cc} is

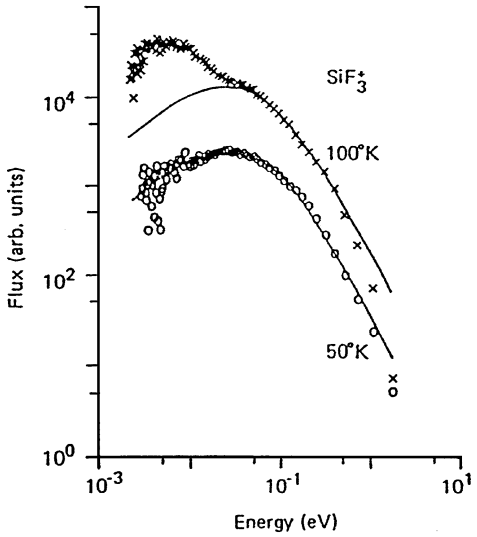

FIG. 5. Kinetic energy distributions of SiF_4 etch products evolved from a silicon surface exposed to 3-keV Ar^+ ions and 5×10^{16} SF_6 molecules/cm^2 s, at two surface temperatures, 50 and 100 K. Solid curves represent collision cascade distributions with a surface binding energy (U_0) of 0.05 eV. (From Osstra *et al.,* 1986.)

a normalization constant, E is the energy (eV), and U_0 is a fitted parameter, termed the "binding energy" of the product. The integral of f_{cc} over all energy is the total flux. The solid lines in Fig. 5 are from cascade theory, and clearly the data fit the theory ($U_0 = 0.05$ eV) for a 50 K surface. At 100 K, however, there is a deviation from cascade theory at low energies. This part of the measurement turns out to fit the Maxwell–Boltzmann distribution, expressed as a flux probability density,

$$f_{MB} = K_{MB} E \exp\left(\frac{-E}{k_B T}\right),$$

where f_{MB} is the fractional probability density distribution (eV m^2 s)$^{-1}$, K_{MB} is a normalization constant, E is the energy (eV), and T is the species temperature, assumed to be the surface temperature. The obvious interpretation of Fig. 5 is that at 50 K, the surface temperature is too low to allow chemically sputtered products to desorb thermally, so only physically sputtered products are observed. However, at 100 K, some of the species that are left in a weakly bound state after the ion impact have equilibrated to the surface temperature and have simply thermally desorbed.

Another important piece of experimental evidence for chemically sputtered products was presented by Winters and Coburn (1992), reproduced here as Fig. 6. These measurements, also made in a vacuum beam apparatus,

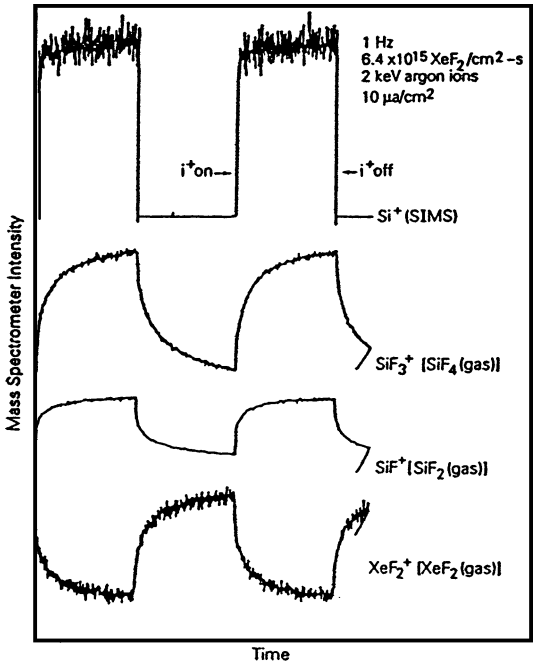

FIG. 6. Mass spectrometric intensity vs time for etch products and reflected XeF_2, with a square wave modulated ion beam. Purely physically sputtered products would have the same time dependence as the Si^+ SIMS signal. The longer time scales evident in the plots for the etch products (SiF_3^+ and SiF^+) suggest chemical sputtering. (From Winters and Coburn, 1992.)

are of various species evolving from a surface exposed to a square wave modulated ion beam and a flux of XeF_2. The Si^+ signal, representing sputtered species, is completely in phase with the ion beam: physically sputtered products leave the surface within 10^{-12} s and therefore no delay in the signal is to be expected. The signals for SiF_3^+ (from dissociative ionization of SiF_4 in the spectrometer), SiF^+ (SiF_2), and XeF_2^+ (XeF_2) all show significant time constants superimposed on the 1-Hz square wave frequency. This is clear indirect evidence for chemically sputtered products that have left the surface long after being created by ion bombardment.

B. Molecular Dynamics Studies of Ion-Assisted Etching Mechanisms

Ion-enhanced etching mechanisms using MD were addressed by Barone and Graves (1995a,b, 1996) in several papers. In the first paper, the Stillinger–Weber potentials were used for Si–Si, Si–F, and F–F interactions. Si–Ar

and F–Ar interactions were modeled with a purely repulsive Moliere pair potential. In the second paper, interactions of both F and Cl were modeled with Si. In this paper, the modified SW potentials proposed by Feil *et al.* (1993). For Cl–Cl and Si–Cl were used.

In the first paper, Barone and Graves (1995a) studied a simplified system: silicon layers with different amounts of prefluorination were exposed to Ar^+ bombardment. The prefluorinated silicon layers were created by adding F atoms at random to the Si lattice during the collision cascade induced by Ar^+ bombardment. Silicon fluoride products that were physically sputtered could easily be detected since they left the layer during the several picosecond trajectory simulation. However, chemically sputtered products would desorb thermally, long after the ion bombardment event occurred. These species were detected by removing SiF_x clusters from the layer one by one and noting the system energy difference before and after their removal. This gives an approximation to the surface binding energy of the clusters. Simple first-order thermal desorption theory was used to determine if the cluster would desorb in the relatively long time between ion impacts. The average time between impact in a layer of area A subjected to an ion flux j_+ is simply $(Aj_+)^{-1}$. The layer areas are of the order of 1000 Å^2 or 10^{-13} cm^2, and typical experimental ion fluxes (even in high-flux plasma etch tools) are usually no more than 10^{17} ions/cm^2 s. This yields a minimum time between impacts of about 10^{-4} s. From thermal desorption theory, if the surface binding energy is less than about 0.8 eV, one would expect the product to desorb before the next ion impacted. Figures 7a and b show the results of the bond energies for various surface species with average F/Si contents of 0.39 and 0.91, respectively. No weakly bound clusters were observed for F/Si $= 0.39$, but significant numbers were found for F/Si $= 0.91$. The weakly bound species in the Stillinger–Weber Si–F and F–F potentials came from F in SiF_x products forming a weakly attractive bond with another F in the layer. Stillinger and Weber had put this weak long-range attraction in their F–F potentials when they were modeling liquid F_2, and this feature remained when they developed the Si–F potentials (Helmer, 1998). From the limited set of simulation results, it is not possible to say if weakly bound products would have been predicted, at least in similar quantities, if this somewhat fortuitous feature in the F–F potential had not been included. However, it suggests that for studies of chemically assisted etching, more quantitative models will require better approximations for the weakly attractive forces responsible for physisorption and the associated processes of diffusion and desorption.

Figure 8 shows the averaged etch yields from each mechanism as a function of the square root of ion energy. The projected threshold for etching is about 5 eV. Figure 9 is a plot of the predicted flux distribution vs

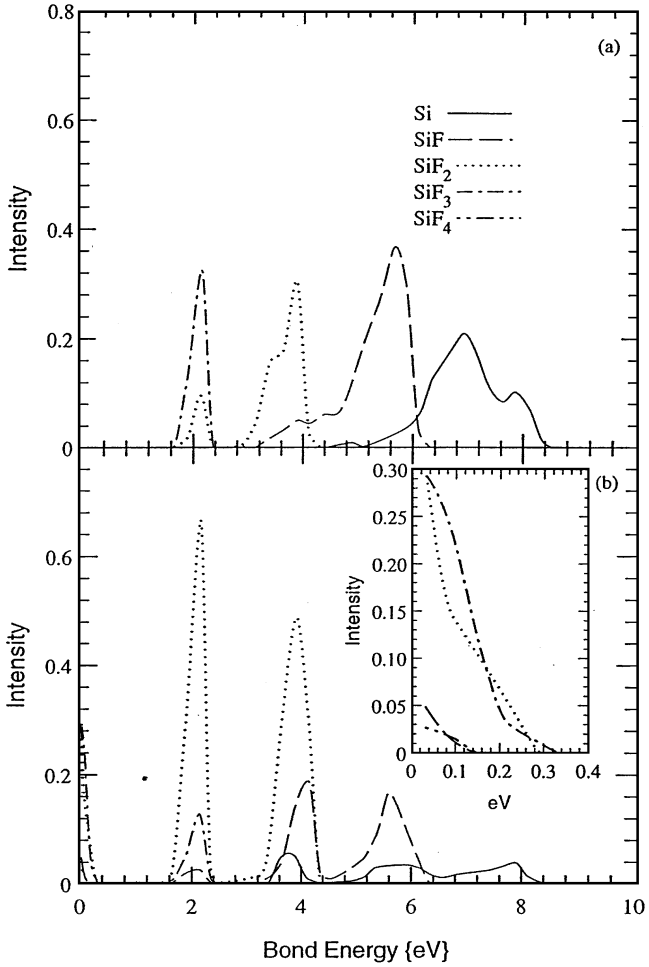

FIG. 7. (a) Bond energy distribution for surface species at the top of the layer with F/Si = 0.39, averaged over 300 impacts, 300 K; (b) Similar distribution for layer with F/*Si* = 0.91. Note the weakly bound species near 0.1–0.3 eV. (From Barone and Graves, 1995a.)

product energy from the simulation, for 200-eV Ar^+ impacting all layers with F/Si > 0.39. The observed sputtered species were SiF, SiF_2, and SiF_3 (symbols), and their energy distribution was fitted with a linear cascade distribution with $U_0 = 0.85$ eV. The dashed, dotted, and dot–dash lines are from calculations of a Maxwell–Boltzmann distribution of etched species, leaving the surface at 300 K, with a yield scaled to the observed ratio of physically sputtered to chemically sputtered species as shown in Fig. 9 . The qualitatitive similarity to Fig. 5 of the measured flux distribution of products

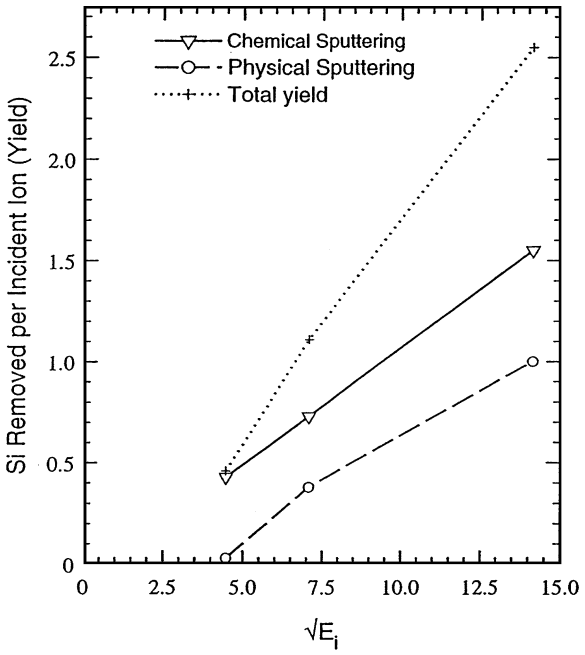

FIG. 8. Etch yield vs ion energy, obtained from averaging MD simulation results, F/Si = 0.91. (From Barone and Graves, 1995a.)

at 100 K is clear: etched products both physically and chemically sputtered would be expected to show a bimodal flux distribution.

These results show that one of the key points in simulating ion-assisted etching is that the Si surface layer must have the proper amount of halogen mixed into it. It does not suffice simply to have the top Si surface coated with a monolayer of halogen. Feil *et al.* (1993) showed that having a monolayer of Cl on Si, then impacting the layer with Ar^+, does not lead to much ion-assisted etching of the underlying Si. The ions mostly sputter the adsorbed halogen, with no increase in Si sputtering—indeed a decrease is often observed in the Si sputtering yield under these conditions. In fact, this point was made by Winters and Coburn (1992), as they concluded that chemically assisted physical sputtering is not generally an important mechanism in ion-assisted etching of Si by halogens. The MD simulations, however, did show that physical sputtering rates can be increased by halogen incorporation, but the halogen needs to be mixed into the Si so as to break Si–Si bonds, thereby weakening the lattice. This raises the question of how to incorporate into the simulation a realistic method to mix the halogen into the layer. Feil *et al.* (1993) proposed that ion bombardment would mix a monolayer of Cl into the

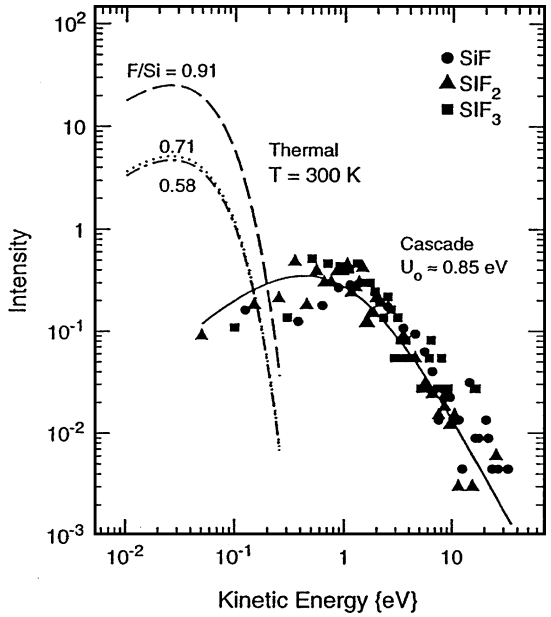

FIG. 9. Kinetic energy distributions for physically sputtered products obtained from the simulation (symbols). Data taken from all simulated layers with F/Si > 0.39 for the chemically sputtering results, represented here as the dashed, dot–dash, and dotted lines, assuming a Maxwell–Boltzmann kinetic energy distribution and 300 K. Solid-line fit to the symbols is collision cascade model with a fitted value of U_0. (From Barone and Graves, 1995a.)

Si, but as noted above, this was not observed. In their second approach to the problem, Barone and Graves (1995b) impacted the Si layer with energetic F or Cl (modeling F^+ and Cl^+). This approach turned out to halogenate the Si near-surface region very rapidly. Indeed, although not emphasized in the original publications, this point is worth stressing: halogen incorporation into Si is most efficiently accomplished through direct halogen ion impact. Direct ion–surface chemistry is important and has probably received less attention than it deserves in the plasma processing community.

In their attempt to study steady state etching of Si by energetic F or Cl, Barone and Graves followed the simulation strategy in Fig. 10. An initially crystalline or amorphised Si layer is impacted with energetic F at normal incidence and some selected energy at a randomly selected lateral location of the top of the layer. Each impact is followed for more than 1 ps, the layer is cooled back to 300 K, weakly bound species are searched for and removed if appropriate, and the statistics are updated. Another random impact location is selected and the process is repeated until it is judged that enough statistics have been collected. It should be noted that there are two stages in the simulation. The first is the approach to a steady-state coverage of halogen.

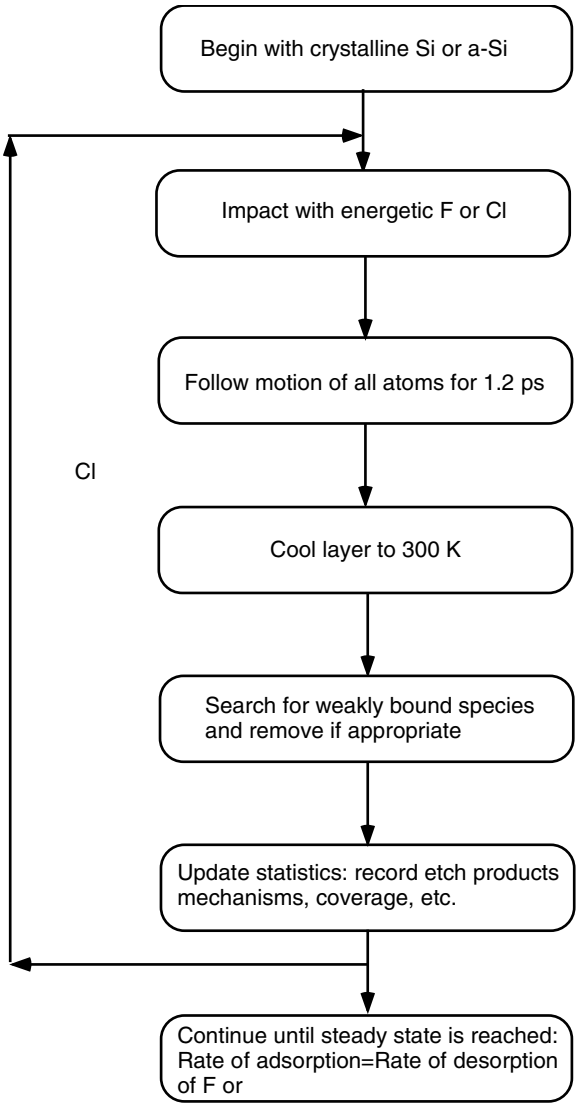

FIG. 10. Simulation strategy for silicon etching with energetic F or Cl. (From Barone and Graves, 1995b.)

Figure 11a shows the average F coverage vs F exposure (in equivalent monolayers), for each of three ion energies. The 10-eV F appears to reach steady-state coverage at about 2 ML after 10- to 15-ML exposure. The 25- and 50-eV ions result in ~3- to 4-ML steady-state coverage. Figure 11b shows the effect of increasing the size of the layer—the fluctuations are reduced with

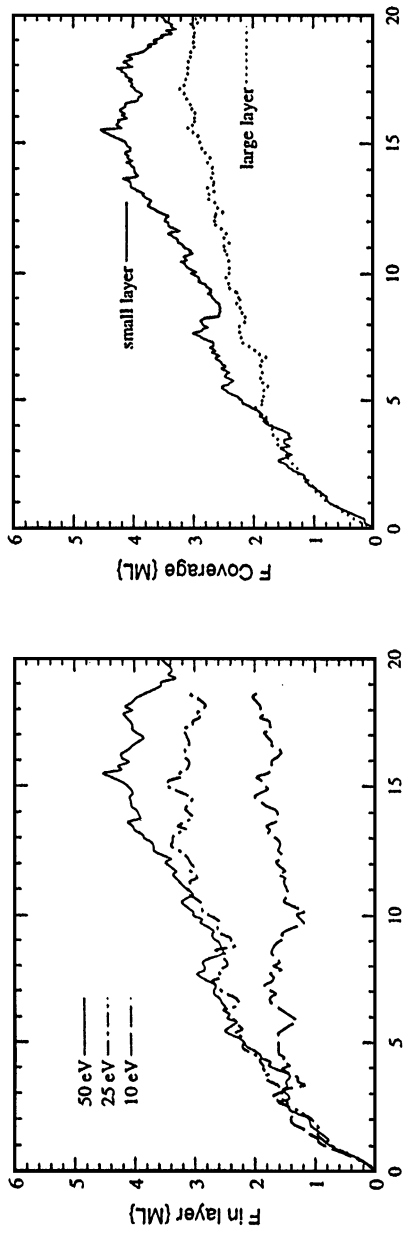

FIG. 11. Fluorine coverage vs F^+ fluence: (a) 10-, 25-, and 50-eV F impact onto smaller layer; (b) comparison of uptake vs fluence for 50-eV F impact onto smaller and larger layer. (From Barone and Graves, 1995b.)

the larger layer but the steady-state coverage appears to be about the same. Figures 12a–d show side views of the layers at various stages of fluorination. Note that the F extends rather deeply into the layer and that the halogen appears to clump in crevices and cracks in the Si lattice. Similar results were obtained with the Cl simulations.

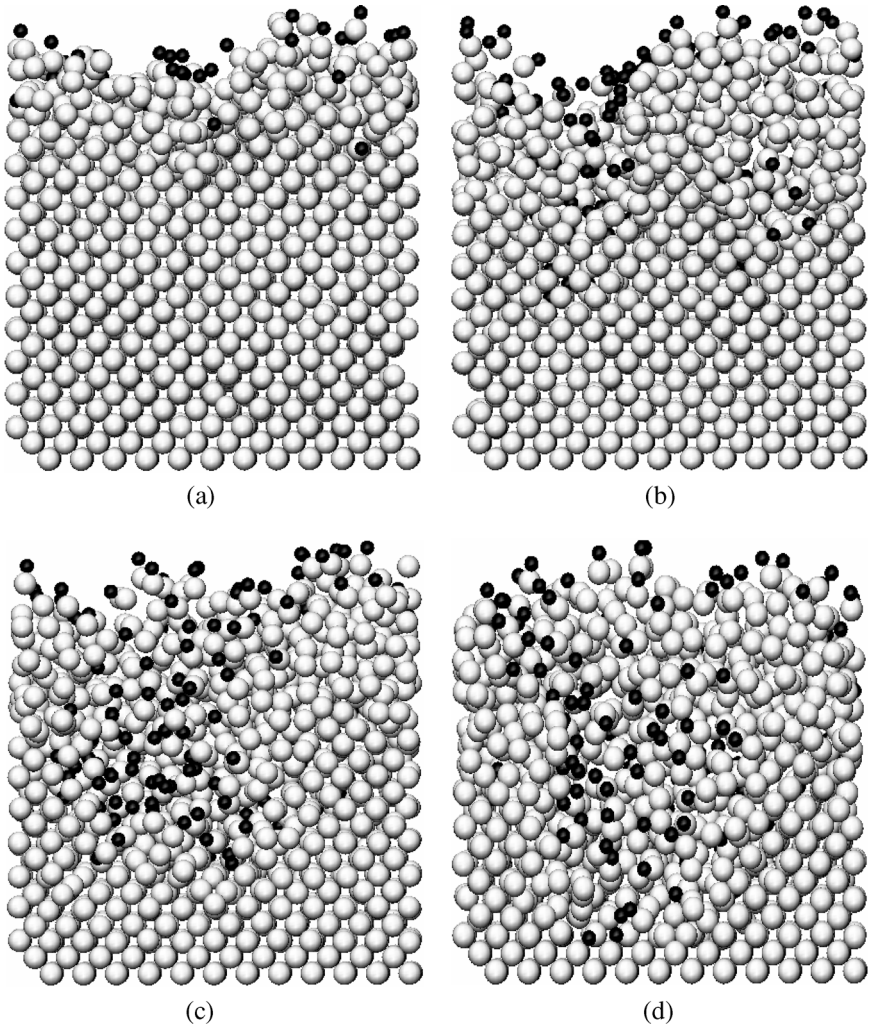

FIG. 12. Evolution of fluorosilyl layer formed from 50-eV F bombardment (a) after 1.39-ML F fluence; (b) after 6.94-ML F fluence; (c) after 13.9-ML F fluence; (d) after 20.8-ML F fluence. (From Barone and Graves, 1995b.)

The second stage of the simulation is to collect enough statistics after the steady-state coverage has been reached so that firm conclusions regarding mechanisms can be established. It turned out that for the cases shown here, chemically enhanced physical sputtering was the dominant form of etching, followed by direct abstraction and chemical sputtering. Direct abstraction is defined to result when the incident reactive species (F or Cl) leaves the surface during the 1-ps collision cascade bound to a Si atom. Sputtering of the adsorbed halogen turned out to be the most important effect limiting the coverage of the halogen at steady state. Other researchers following similar simulation strategies obtained similar results, although quantitative results differed (Athavale and Economou, 1995; Hanson *et al.,* 1997, 1998).

To summarize this section, let us attempt to put the results of these simulations and experiments into some perspective. MD simulations, using approximate semiempirical classical interatomic potentials, have been shown to be very valuable in studying details of events occurring during the rapid collision cascade following ion impact. The major qualitative results of etch mechanisms identified by experimentalists were confirmed by the simulations. However, the simulations provided valuable additional details of the processes. This includes observations such as the much greater rate of halogen incorporation from energetic halogen ions compared to adsorbed halogen impacted by rare-gas ions, the depth and spatial distribution of halogen in the Si near-surface, and the dynamic events leading to steady-state coverage. The side view of the mixed layer of Cl and Si illustrated in Figs. 13a–d can be compared with the view proposed by Layadi *et al.* (1997) (Fig. 3b) in their interpretation of the near-surface silicon region exposed to a chlorine plasma. Furthermore, movies made of trajectories and of layer evolution were found to be very useful for visualizing the relevant processes. It may be that the biggest contribution to the plasma processing research community from MD simulations has been the unprecedented opportunity to develop intuition of dynamic events at surfaces exposed to reactive plasmas using visualization of multiple trajectories.

C. Ion–Surface Scattering Dynamics

As noted above, plasma processing in semiconductor manufacturing generally involves ion and neutral interactions with submicron features. Ions accelerated across the plasma sheaths impact the wafer surface at near-normal incidence but encounter topography at the feature level. This is illustrated in Fig. 14. The ion impacts both the feature bottom and the sidewall. The ion reflects from the sidewall with some energy and angle before striking another part of the feature. If one is interested in predicting the shape evolution occurring during etching, then information about ion reflection is

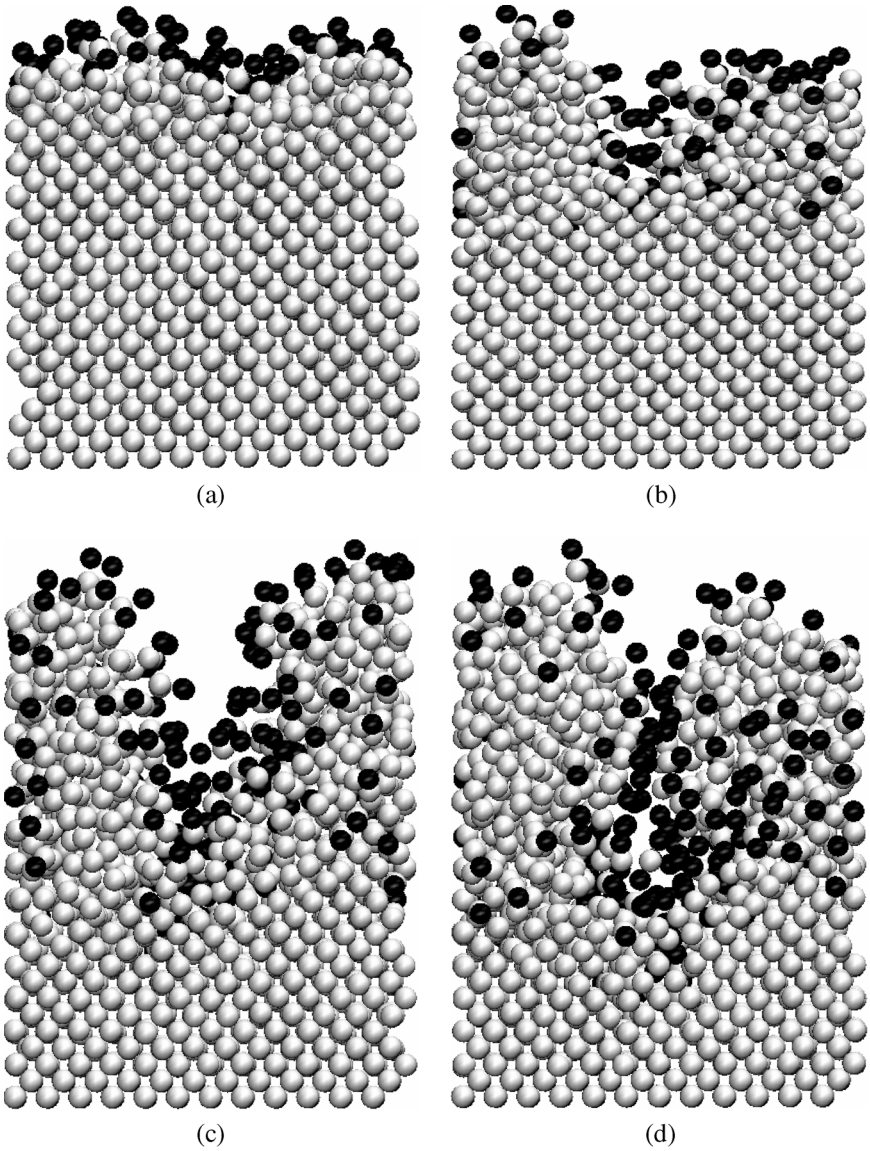

FIG. 13. Evolution of chlorosilyl layer from 50-eV Cl bombardment (a) after 1.39-ML Cl fluence, (b) after 7.9-ML Cl fluence, (c) after 13.9-ML Cl fluence, and (d) after 20.8-ML fluence. (From Barone and Graves, 1995b.)

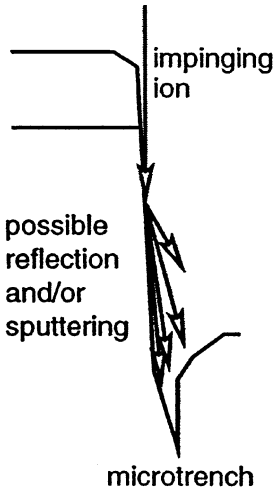

FIG. 14. Schematic of ion impact and scattering on feature sidewall and bottom during plasma etching.

necessary. Indeed, as the feature aspect ratio (depth to width) increases, sidewall interactions become more important. Most profile simulators have simply assumed either that ions reflect at the specular angle, with no loss of kinetic energy, or that reflecting ions are ignored. Both assumptions can introduce significant errors into profile shape evolution models. MD simulations offer an opportunity to study systematically the nature of ion reflection from surfaces. This section focuses on two aspects of ion reflection: the role of atomic-scale roughness and the use of elastic binary collision theory as an approximate model for ion reflection from feature sidewalls.

1. Ion–Surface Scattering: Role of Surface Roughness

The model surfaces chosen for this study are shown in Figs. 15 and 16. A bare silicon surface, a silicon surface with a single monolayer of Cl chemisorbed (Fig. 15), and a silicon surface with about 2.3 monolayers of Cl mixed into the top $\sim$20 Å were chosen (Fig. 16). The potentials were Feil–Stillinger–Weber, and the simulations are described by Helmer and Graves (1998). For the results shown here, Ar^+ and Cl^+ are used as the incident ions.

The coordinate system we use for the ion scattering trajectories is shown in Fig. 17. The incident angle is defined with respect to the surface normal, and is denoted θ_i, with the reflected polar angle θ_r and reflected azimuthal angle ϕ_r. It is necessary to impact the ion many times on a given surface, varying the impact location each time and collecting statistics on the scattering event at a given incident energy, angle, ion type, and surface. For

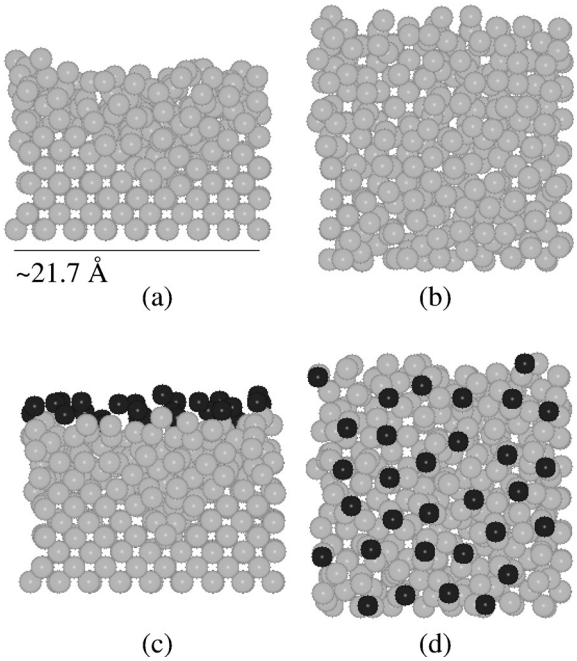

FIG. 15. Side and top views of two surface layers: (a) bare Si (side); (b) bare Si (top); (c) 1-ML Si–Cl (side); (d) 1-ML Si–Cl (top). (From Helmer and Graves, 1998.)

each incident ion, the reflected (neutralized) ion comes off at a different (in general) energy and angle. We display the results of these trajectory simulations in several ways. The first is illustrated in Fig. 18, from simulations of an Ar^+ ion (85° from normal incident angle) impacting a bare silicon surface at 50 eV. In Fig. 18a, each of the several hundred trajectory simulations is represented as a dot on the polar plot. Each dot on the plot represents a separate trajectory. The scatter plot of several hundred trajectories gives an idea of the distribution of reflected energies and angles. The radial lines represent the fraction of incident energy retained by the incident ion, so that the outermost radial line corresponds to an E_r/E_i (the ratio of reflected-to-incident ion energy) $= 1$. The origin corresponds to an $E_r/E_i = 0$. In this plot, the polar angle θ_r is shown projected on the incident plane defined by the ion vector and the z axis, and therefore no information about azimuthal scattering is shown. A specular reflection would result in a scattering angle equal to the incident angle (85°), with no loss of incident energy, so the dot would be on the outer radial line at 85°. Figure 18a shows that a number of trajectories come close to being specular. Data on the distribution of azimuthal angles ϕ_r are shown in Fig. 18b, projecting the reflected ion exit trajectory vector onto the surface—viewing from "above," so to speak.

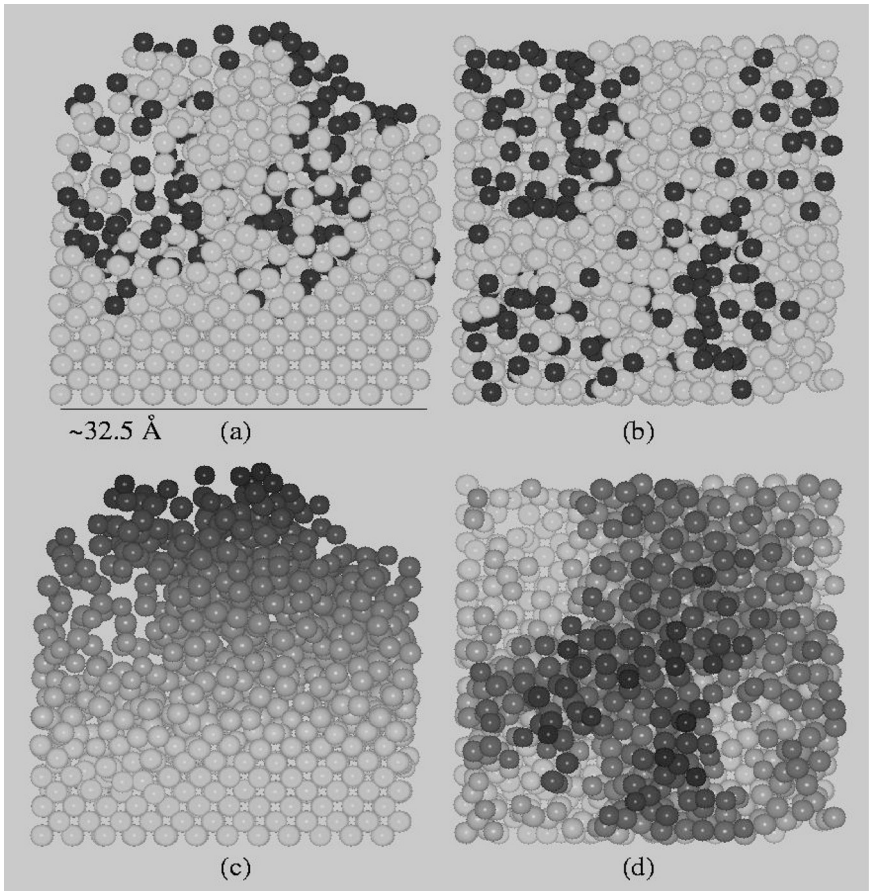

FIG. 16. Views of 2.3-ML Si–Cl surface layers: (a) side view; (b) top view—gray spheres Si, dark spheres Cl atoms; (c) side view with atoms shaded according to vertical position; (d) top view with depth shading. (From Helmer and Graves, 1998.)

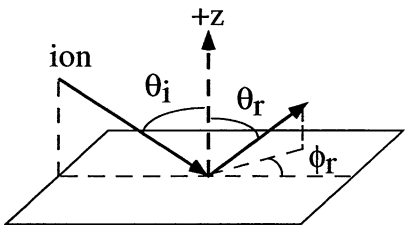

FIG. 17. The coordinate system and angle definition: incident, Θ_i; reflected polar, Θ_r; and reflected azimuthal, ϕ_r. (From Helmer and Graves, 1998.)

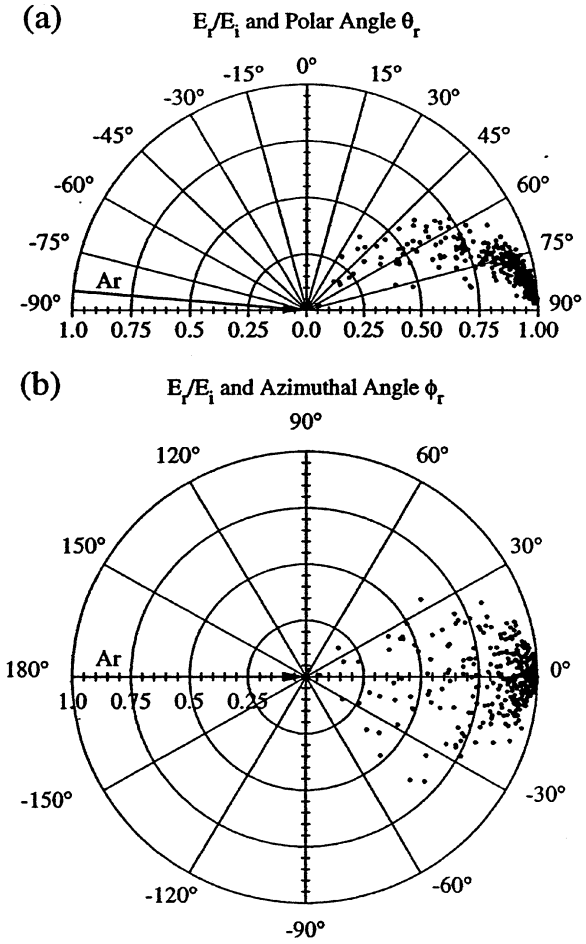

FIG. 18. The angles and reflected energy fractions of Ar reflected from a bare Si surface: (a) E_r/E_i; Θ_r; and (b) E_r/E_i; Θ_r. Each point represents the result of a single impact with $E_i = 50$ eV and $\Theta_i = 85^\circ$. (From Helmer and Graves, 1998.)

It can be seen clearly from these figures that even at an 85° incident angle and on a fairly smooth surface, there is a significant amount of nonspecular scattering. Figures 19a and b illustrate the effects of polar angle scattering from the 1-ML Cl-covered Si surface and the 2.3-ML covered surface, respectively. In these plots, a Cl^+ ion is used at 50-eV incident energy and an 85° angle of incidence. Scattering from the relatively smooth 1-ML surface is fairly specular, but scattering data from the rougher surface show a big deviation from specular. The main point to be drawn from these limited

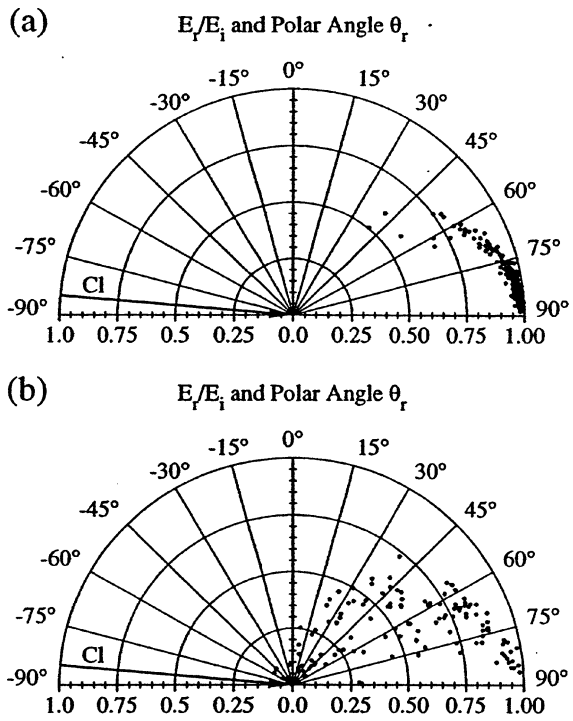

FIG. 19. Polar angles and reflected energy fraction of the Cl reflected from the (a) 1-ML Si–Cl surface and (b) 2.3-ML Si–Cl surfaces. (From Helmer and Graves, 1998.)

examples is that the state of the surface—especially its roughness—will significantly affect scattering, even at near-oblique incidence angles such as 85°. The consequences for profile evolution have been examined for several cases of practical interest, but those results are not presented here (e.g., Vyvoda *et al.,* 1999; Vyvoda, 1999). It is important to recognize that feature shape evolution models must take into account surface roughness and other variables affecting scattering such as the identity of the incident ion, the composition of the underlying material, and any species adsorbed near the surface. This adds to the already very challenging task of constructing self-consistent, quantitative feature profile evolution models. Indeed, the MD simulations demonstrate that whenever any of the relevant variables change (ion type, ion energy, angle of incidence, and surface composition or roughness), the scattering results in general change significantly. While it is not difficult to amass huge amounts of scattering results from trajectory simulations, there are few theories with which we can interpret and digest these data. One approach that has shown some success and may form the basis for future attempts to simplify this problem is described next.

2. Ion–Surface Scattering: Binary Collision Theory

If one assumes that the ion–surface interaction can be described in terms of one (or two) binary, elastic collisions between isolated bodies, some simplifications of the ion scattering problem can be made. Of course, the accuracy of the approximation may be checked by comparing them to MD simulations. Details of this theory and its application to ion–surface scattering can be found elsewhere (Helmer and Graves, 1998; Helmer, 1998), but a brief synopsis is provided here. A relation between the scattered ion energy and the angle can be obtained by equations that represent conservation of linear momentum and kinetic energy, assuming that no energy is lost to electronic excitation (an excellent approximation for the conditions of interest here). The results are presented in terms of the total scatter angle α rather than the polar and azimuthal angles. The total scattering angle is the angle the scattered ion takes from the projected incident angle vector. A total scattering angle of 0° would correspond to the ion continuing on its initial trajectory. Note that for the case of an ion grazing the surface at an 85° incident angle, a total scattering angle of 10° represents specular scattering. One parameter in the model is the ratio of the ion mass to the surface atom mass μ. For Ar^+ on Si, $\mu = 1.43$, and for Cl^+ on Cl-covered Si, $\mu = 1.0$.

Figure 20 shows a plot of the energy fraction versus the total scattering angle for several cases. Note that binary collision (BC) theory simply relates

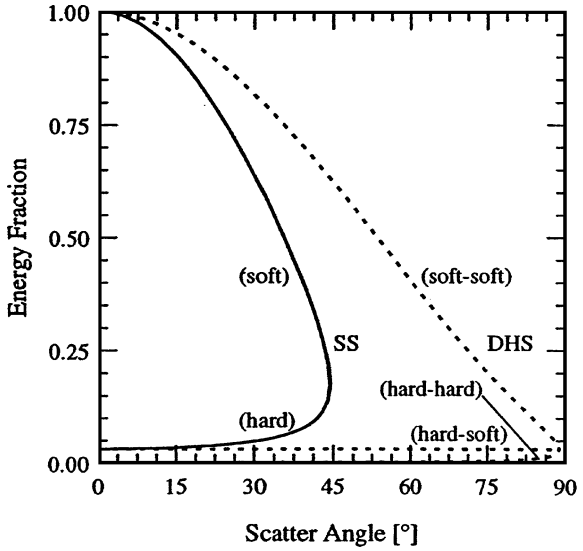

FIG. 20. The reflected energy fraction is shown as a function of the total scatter angle for both the single-scatter and the double half-scatter BC models. Mass ratios $\mu = 1.43$. (From Helmer and Graves, 1998.)

the energy fraction retained in the scattering ion and the angle of scattering. It says nothing about the distribution of scattering angles. The solid line denoted SS represents a single binary collision, with the two branches indicating a "soft" collision and a "hard" collision. Extension of this to two collisions, each of which scatters the ion through half of the total scattering ["double half-scatter" (DHS)], is also shown in Fig. 20, with three branches: two "soft" collisions (soft-soft), a hard and a soft collision (hard–soft), and two hard collisions (hard–hard). For the cases considered here, with ions impacting at energies between 20 and 100 eV, for Ar^+ and Cl^+ onto bare Si and Cl-covered Si, the MD results tended to be between the theoretical results from BC theory assuming a single soft collision and those assuming two soft collisions in double half-scattering. This is shown in Figs. 21a and b. Figure 21a is for the case Ar^+, 50 eV, 85°, and bare Si. The histogram plots the relative frequency, and the symbols are from the MD simulations providing the average E_r/E_i as a function of the scatter angle. The data lie in the region between SS and DHS results. Figure 21b shows the same results for the rough surface (Cl^+, 50 eV, 85°, 2.3-ML Cl). The histogram of scatter angle frequency shows a broader scatter angle distribution, as shown previously for the same data plotted in Fig. 19b. It also demonstrates that the MD data fall between the SS and the DHS results using BC theory. Of course, the relatively good agreement between the MD and the BC theory results does not imply that the collisions are truly binary—detailed analysis of the ion trajectories in the MD simulations indicates that some trajectories were dominated by a single encounter, but many others were not. Nevertheless, the simplifications offered by BC theory make it attractive for future efforts to simplify profile evolution codes while retaining some physics and avoiding complete reliance on nonphysical adjustable parameters. One must, of course, come up with some procedure to select the distribution of scattering angles to use this theory.

D. Ion–Surface Interactions with both Deposition and Etching: CF_3^+/Si

In this section, we return to the question of ion-assisted etching mechanisms, but now with the added complication of having a component of the incident ion (C) that is depositing as well as a component (F) that tends to etch the surface material. This situation is actually quite common in practical etching applications because it is often necessary to have such a depositing species to promote etch selectivity. The best-known and most widely used example is fluorocarbon-containing plasmas used to etch dielectric materials, such as SiO_2 and Si_3N_4, but that must be selective with respect to a layer

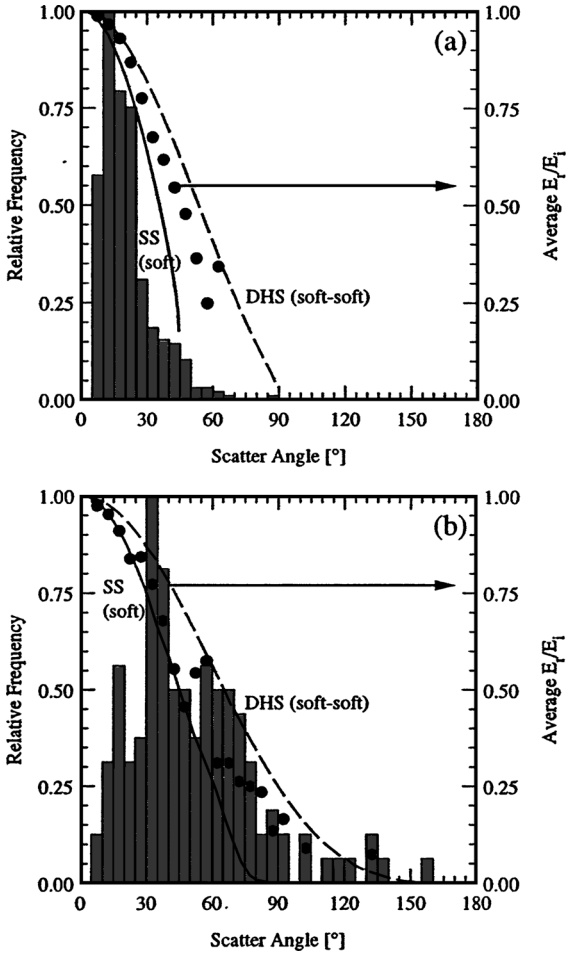

FIG. 21. The histograms show the distributions of total scattering angle a for the reflected atoms. (a) Ar^+, 50 eV, 85°, bare Si; and (b) Cl^+, 50 eV, 85°, 2.3-ML Si–Cl. Filled circles represent the average reflected energy fraction corresponding to the reflection angle. Single-scatter (SS) soft–soft branch and double half-scatter (DHS) soft–soft branch model predictions for (a) $\mu = 1.43$ and (b) $\mu = 1.0$ also shown for comparison with E_r/E_i data from simulation. (From Helmer and Graves, 1998.)

of silicon below the dielectric film. For SiO_2 etching, fluorocarbon plasmas often work well because the C in the incident ion is volatilized by the O in the film, and the Si by the F in the incident ion. Of course, in plasma reactors, neutral species play an important role as well, but many of the same principles hold for neutral chemistry. To simplify matters, we consider just the case of fluorocarbon ions onto silicon surfaces. In this case, the C in the incident

ion tends to be more depositing, and even if the net effect is etching, the etch rate of the underlying Si tends to be slower with C present. A plasma etch chemistry that etches the overlying SiO_2 film readily, but the underlying Si film more slowly, is often desirable in practice. A similar situation can also occur when etch products (e.g., silicon chlorides or fluorides) are ionized in the plasma and return to the surface. The silicon tends to be depositing and the halogen tends to etch. The net effect can be either deposition or etching, depending on the conditions. It was the purpose of the studies summarized here to attempt to learn more about the mechanisms that govern such situations, at least under fairly idealized conditions.

In this case, partly because carbon can form many kinds of bonds with halogen and silicon (sp, sp^2, sp^3), the Stillinger–Weber interatomic potentials were replaced by a set of potentials developed originally by Brenner (1990, 1992) for the carbon–hydrogen system. Tanaka *et al.* (2000) describe the procedure used to modify the parameters in the C–H system to C–F. Abrams describes the development of this set of interatomic potentials (Abrams and Graves, 1999; Abrams, 2000), including the addition of Si to allow studies of C–F–Si atoms interacting. The simulation procedures followed here are very similar to those described earlier and are treated in much greater detail elsewhere (Abrams and Graves, 1999, 2000a–d; Abrams, 2000). Abrams reports on a comparison between the different forms of potentials for several cases in which some overlap exists. In all cases, qualitative results are robust, but quantitative results generally differ with different forms of the potential energy function or when parameters within any given set are altered. This is, of course, to be expected. In this section, results from MD simulations of CF_3^+ onto silicon surfaces are reported, including the development of a steady-state etching layer, and some information that can be compared to experiment.

1. CF_3^+ Etching of Silicon

In the simulations described here, an initially bare Si layer of 512 atoms, with a lateral area of about 500 Å^2 and a depth of about 20 Å, was used. Periodic lateral boundaries and a fixed bottom layer were used as before. The top Si layer was "amorphized" by repeated impacts of 200-eV Ar before exposure to CF_3^+. The goal was to simulate an ion beam experiment in which a beam of monoenergetic CF_3^+ is directed at a silicon surface, with no other species impacting the surface. The initial transient associated with the buildup of a mixed C–F–Si layer at the surface would be followed by a period of steady-state etching in which the composition and thickness of the top mixed layer would not change. Each ion impact was followed for 0.2 ps, and tests were made to be certain that the results did not depend on the length of the impact trajectory time. Clusters of material that were weakly

bound to the surface were identified and removed between ion impacts, and species that desorbed during the 0.2-ps trajectory simulation or that were retained within the layer that were strongly bound were recorded. Again, the assumption is made that the only thing that happens between the relatively infrequent ion impacts is the thermal desorption of weakly bound clusters (of any size) and dissipation of the heat added by the ion bombardment. Of course, this is not strictly correct since some species will diffuse and/or react during this time, but since the layer returns to room temperature very quickly after the ion impact, any thermally activated processes are likely to be relatively slow. In any case, this is the simplest set of assumptions that seem consistent with the major identified processes and is therefore a reasonable place to begin the study.

Figures 22 and 23 illustrate the simulated evolution in C, F, and Si content of the layers for 100-eV CF_3^+ impacts at normal incidence, as a function of ion fluence (Abrams and Graves, 1999). Ion fluence is simply the product of ion flux and time, or the number of ions that have hit the simulated surface. Sometimes the unit of monolayer is used, which refers to a number of ions equal to the number of atoms in the topmost layer. These figures also show the statistical repeatability of three runs, including results from a cell with twice the surface area ($\sim$1000 Å^2). It can be clearly seen from Fig. 22 that C and F build up rapidly, with an initial sticking probability of unity, then after a fluence of 500 impacts (equivalent to about 10 monolayers or 10^{16} ions cm^{-2}), the layer composition reaches steady state. Later, evidence is

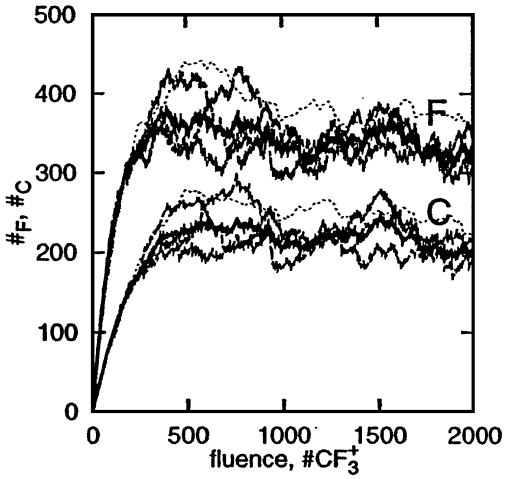

FIG. 22. The content of C and F as a function of the 100-eV CF_3^+ ion fluence. The narrow curves denote each statistically equivalent data set, while the thickest curve is the average. The dotted curve is data from the larger (1000-Å^2) surface, scaled by a factor of 0.5 in both dimensions, and is not included in the average. (From Abrams and Graves, 1999.)

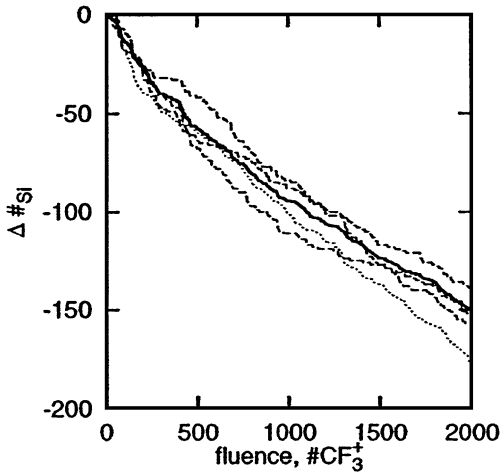

FIG. 23. The change in Si content of the surface as a function of the ion fluence. The thickest curve is the average of the three data sets. At steady state, the slope of this line is the etch yield of Si, 0.06 Si/ion. The dotted curve is data from the larger (1000- Å^2) surface, scaled by a factor of 0.5 in both dimensions, and is not included in the average. (From Abrams and Graves, 1999.)

presented that the F content of the layer governs the C and F saturation characteristic shown in Fig. 22. Figure 23 shows that the Si content of the layer drops at a rate corresponding to an etch yield (Si atoms per incident ion) of 0.06—a relatively low yield. A snapshot of the atomic configuration in the cell after 1000 ion impacts at 100 eV and normal incidence is presented in Fig. 24. The top 20 Å or so consists of a mixed "fluorocarbosilyl" layer over essentially pure Si. The net silicon etching must occur from Si moving up from below, leaving the top of the layer after mixing in the fluorocarbon material that forms there. This result is in qualitative agreement with the experimental measurements by Coburn *et al.* (1977), Thompson and Helms (1990), and Sikola *et al.* (1996). It appears that the MD simulation at least qualitatively reproduces the behavior of steady-state Si etching through a fluorocarbon overlayer.

The role of CF_3^+ ion energy in the composition profiles of C, F, and Si is shown in Figs. 25a–d (Abrams and Graves, 2000d). Figure 25a corresponds to an ion energy of 25 eV, and the thickness of the C and F overlayer can be seen to be about 5–10 Å. The Si extends into the mixed F and C region. As energy is increased, up to 200 eV (Fig. 25d), several trends emerge. The F appears to be reduced near the surface, peaking deeper into the layer than the C. In addition, the mixed layer thickness has increased from 5–10 to about 15 Å or more. The Si profile is accordingly more spread out, and the F/C ratio in the mixed layer has decreased from about 2.5 to 1.5.

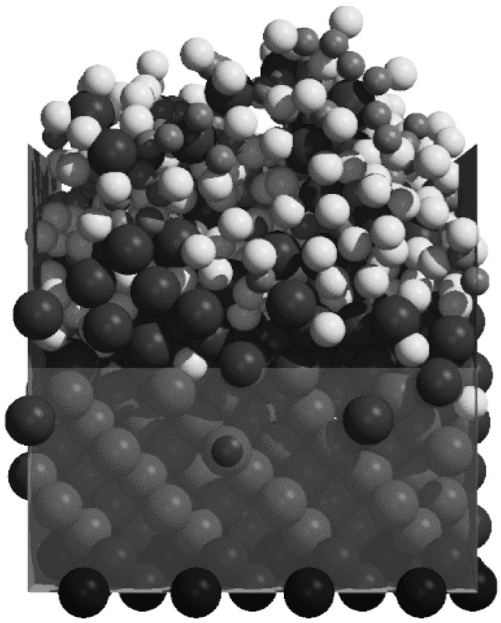

FIG. 24. Snapshot of the atomic configuration after a fluence of 1000 CF_3^+ at 100 eV and normal incidence. A side view is shown, with the positive z-direction up and the positive x-direction right. The periodic transverse boundaries of the cell are rendered as translucent planes; the boundary facing the viewer is cut away. Si, dark gray; C, gray; F, white. (From Abrams and Graves, 1999.)

Figure 26 plots the etch yield (Si atom/ion) and C layer thickness as a function of ion energy from 25 to 200 eV. The etch yield can be fit to the commonly used phenomenological form with a square root dependence on ion energy and a threshold energy. Results from the larger cell, showing little cell dependence, are also shown in Fig. 26.

These results seem characteristic of many ion-assisted etching systems that contain depositing material (C in this case). Initially, the C and F build up rapidly in the top 10–15 Å of the Si surface, mixing with the underlying Si. As the F content increases, the sticking probability decreases, until as much C and F is removed as is deposited. Under these conditions, some Si from the underlying layer is also lost. As shown later, it is possible (for example, with CF^+) that the fluorocarbon film continues to build and steady-state deposition occurs rather than etching. The key seems to be what near-surface composition corresponds to a steady state, given the ion type, energy, angle of impact, and underlying material. In the case of CF_3^+, there is enough F coming in with the ion that steady state requires Si to be mixed into the near-surface

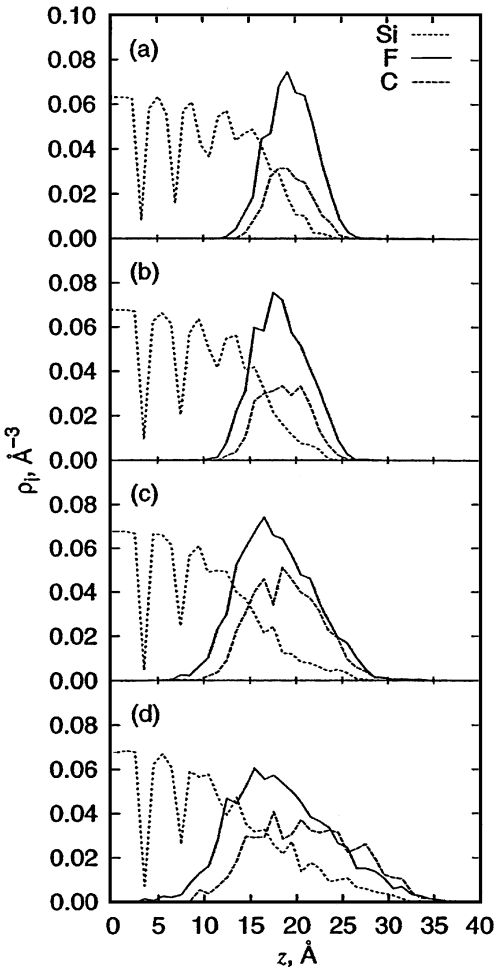

FIG. 25. Depth profiles for Si, F, and C after a fluence of 2×10^{16} ions/cm^2 CF_3^+ (1000 impacts) for E_i = (a) 25 eV, (b) 50 eV, (c) 100 eV, and (d) 200 eV. $z = 0$ corresponds to the simulation cell bottom. (From Abrams and Graves, 2000d.)

composition. This of course corresponds to etching, and to a balance between impacting C and F and C and F being removed. In ion-induced deposition, the impacting ion cannot remove all of the material deposited, and a film builds up.

2. Product Distributions in CF_3^+ Etching of Silicon

A common problem in modeling plasma tools is determining what is coming from walls bounding the plasma. Molecular gases entering the tool

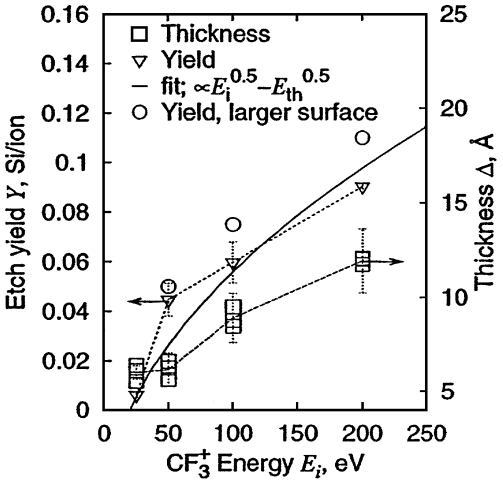

FIG. 26. Etch yield Y and fluorocarbosilyl layer thickness Δ vs CF_3^+ ion energy E_i. The error bars in layer thickness denote the average fluctuation in this quantity during steady state. Etch yield error bars denote the standard deviation among three independent runs. The solid curve is a best fit of $Y = a(E_r^{0.5} - E_{th}^{0.5})$, where $E_{th} = 25$ eV and $a = 0.01$ ($eV^{-0.5}$). Circles are from single runs on a surface with twice the lateral surface area to show the effects of cell size. (From Abrams and Graves, 2000d.)

can be dissociated, and these dissociation products can react in the gas phase and at surfaces. In addition to these sources of chemical species in the plasma, ion impact at surfaces induces a considerable flow of neutral species back into the gas phase. Etch products (i.e., species containing Si that leave the surface) are an obvious example, and it is well known that etch products can play a very important role in plasma tool chemistry. For one thing, these species, or those derived from them by dissociation or ionization, can return to the wafer surface and redeposit. In some cases (depending on applied power, gas pressure, and flow rate among other variables), the flow of material from walls can match or even exceed gas flow into and out of the plasma reactor. Little is known or understood about how ions, especially reactive molecular ions, contribute to this mass flow from walls. The results in this section provide some insight into surface emission product composition and kinetic energy distributions from CF_3^+ impacts onto Si. Of course, in a real tool, many types of ions, in addition to many neutral species, would impact the surface, not just CF_3^+. However, examination of this simpler, but reasonably representative case should prove helpful.

Table II summarizes the majority of species removed from Si surfaces under CF_3^+ impact at energies of 25–200 eV (Abrams and Graves, 2000c). Stastistics were collected after the surfaces reached steady state. The table lists the average yields (number per incident ion) and standard deviation.

TABLE II
BREAKDOWN OF MAJOR SPUTTERED SPECIES AS AVERAGE YIELD PER ION DURING STEADY-STATE ETCHING FOR ION INCIDENT ENERGIES OF 25, 50, 100, AND 200 eV[a]

	Yield per ion ± SD			
Molecule	E_i = 25 eV	E_i = 50 eV	E_i = 100 eV	E_i = 200 eV
F	0.051 ± 0.005	0.482 ± 0.012	0.987 ± 0.012	1.240 ± 0.020
F_2	0.001 ± 0.001	0.088 ± 0.002	0.270 ± 0.010	0.282 ± 0.011
C	0.000 ± 0.000	0.000 ± 0.000	0.023 ± 0.004	0.067 ± 0.003
CF	0.001 ± 0.001	0.067 ± 0.008	0.192 ± 0.017	0.217 ± 0.006
CF_2	0.085 ± 0.008	0.484 ± 0.010	0.275 ± 0.006	0.180 ± 0.006
CF_3	0.739 ± 0.005	0.211 ± 0.005	0.036 ± 0.003	0.017 ± 0.001
CF_4	0.091 ± 0.001	0.063 ± 0.005	0.012 ± 0.001	0.006 ± 0.001
C_mF_x	0.022 ± 0.002	0.046 ± 0.003	0.116 ± 0.005	0.118 ± 0.003
m	2.15 ± 0.03	2.34 ± 0.03	2.56 ± 0.06	2.47 ± 0.05
x	5.13 ± 0.05	3.70 ± 0.13	2.45 ± 010	1.99 ± 0.06
SiF	0.000 ± 0.000	0.000 ± 0.000	0.003 ± 0.002	0.009 ± 0.002
SiF_2	0.000 ± 0.000	0.002 ± 0.001	0.007 ± 0.003	0.017 ± 0.003
SiF_3	0.000 ± 0.000	0.008 ± 0.001	0.012 ± 0.003	0.019 ± 0.003
SiF_4	0.000 ± 0.000	0.014 ± 0.003	0.012 ± 0.002	0.013 ± 0.004
SiC_mF_x	0.006 ± 0.001	0.019 ± 0.002	0.019 ± 0.002	0.023 ± 0.002
m	1.62* ± 0.25	1.68 ± 0.17	1.89 ± 0.15	1.88 ± 0.10
x	7.20 ± 0.51	5.91 ± 0.31	4.51 ± 0.15	3.47 ± 0.21
SiC_nF_x	0.000 ± 0.000	0.001 ± 0.001	0.004 ± 0.001	0.005 ± 0.001
n		4.39 ± 2.56	7.10 ± 0.67	6.81 ± 1.07
x		7.11 ± 4.27	7.34 ± 0.64	5.19 ± 0.33

[a]High molecular weight molecules were split into groups according to $1 < m < 5$ and $n > 4$, and average stoichiometries of these groups are given. Errors given are standard deviations among the four runs (Abrams and Graves, 2000c), except that only three runs were done for $E_i = 25$ eV.

Figure 27 shows a series of plots for each of the main C- and F-containing products leaving the surface as a function of the ion energy, as well as the total yield for that species. The main ejection mechanisms are sputtering (S), reflection (R), and abstraction (A). As ion energy increases, the dominant ejection mechanism shifts and is different for different species. At 25 eV, the main product leaving the surface is simply reflected CF_3. As energy is raised to 50 eV, the ion fragments more on impact and CF_2 and F replace CF_3 as the main species. By 100 eV, about half of the incoming C leaves the surface in the form of CF and CF_2. F and F_2 also leave the surface with a yield of 1 and 0.25, respectively. Furthermore, a significant fraction of these species is from sputtering and abstraction, not reflection. In other words, the ejected F, F_2, CF, and CF_2 were part of the surface before the ion impact. There is mixing and exchange with the surface, and material leaving the surface is not simply reflected ions. Of course, under steady-state

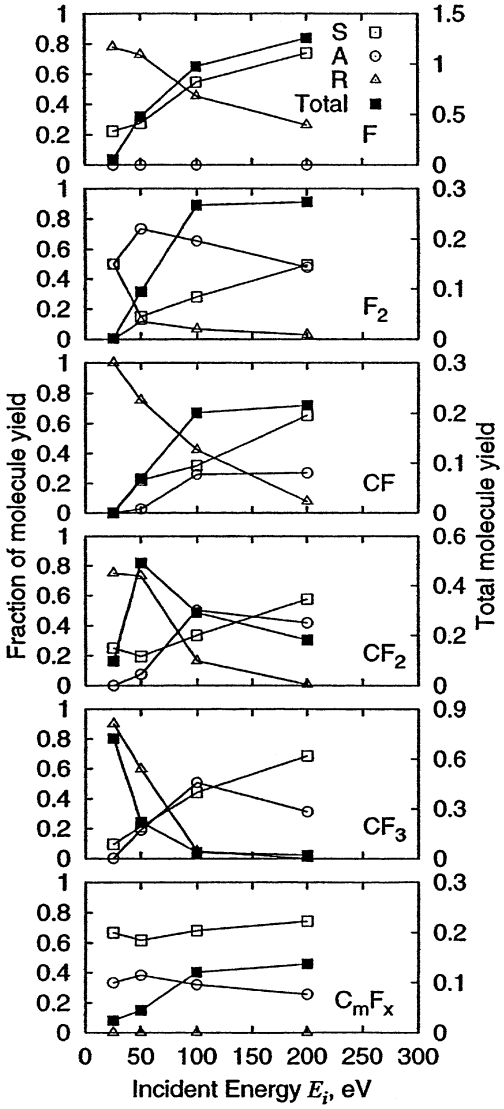

FIG. 27. Yields of major products F, F_2, CF, CF_2, CF_3, and C_mF_x vs E_i. Filled symbols are the total yield (molecules/ion), and open symbols are the fraction of the total yield resulting from each mechanism: sputtering (S), abstraction (A), and reflection (R). (From Abrams and Graves, 2000c.)

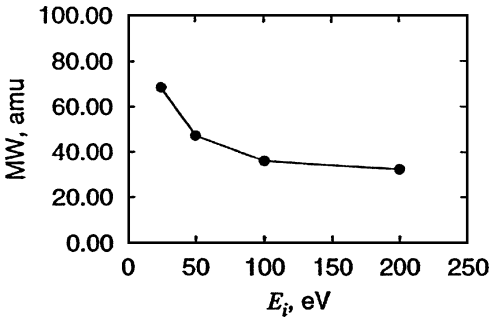

FIG. 28. Average product molecular weight vs E. The standard deviations are smaller than the symbol size. (From Abrams and Graves, 2000c.)

conditions, on average 1 C and 3 F must leave the surface per incident CF_3. By 200 eV, the main ejected species is F.

Figure 28 is a plot of the average product molecular weight as a function of ion energy. Obviously, as energy increases, the average size of the ejected species decreases. However, a careful examination of Table II indicates that the higher molecular weight products increase as the energy increases as well, and these relatively few but heavy species can contain a significant fraction of the C and F emitted from the surface.

From the point of view of etched feature profile evolution, two other characteristics of the ejected species are important: the energy and angle of ejection of products. The product kinetic energy distributions for the set of cases we have examined in this section are shown in Fig. 29. As energy increases from 25 to 200 eV, the primary ejection species changes from CF_3 to F. The solid line corresponds to linear cascade theory (LCT), and as ion impact energy increases, the total kinetic energy distribution gets closer to this model. The average kinetic energy of the ejected species as a function of ejection angle is shown in Fig. 30. An angle greater than 90° corresponds to species moving into the surface at the end of the trajectory. Note that most species are ejected with an average energy of 1 eV and at an angle that peaks around 50° from normal. Species that leave the bottom of an etched feature are more likely to impact the sidewalls than they are simply to move straight up the feature. In addition, a species leaving with 1 eV corresponds to a temperature of about 10^4 K and, therefore, is capable of scaling a significant activation energy barrier for a subsequent chemical reaction.

3. CF^+ and CF_2^+ Deposition on Silicon

As noted above, under some conditions, fluorocarbon ions will deposit as a film rather than etch the underlying silicon. Since C is the depositing species and F the etching species, by reducing the F/C ratio in the ion, one

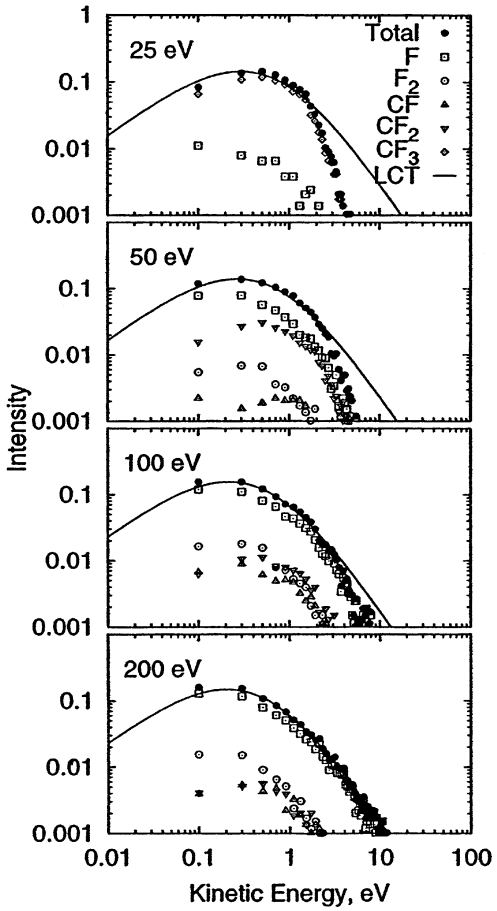

FIG. 29. Product kinetic energy distributions for $E_i = 25$, 50, 100, and 200 eV. The solid line is a best fit to the "total" distribution using linear cascade theory (Sigmund, 1969). (From Abrams and Graves, 2000c.)

moves in the direction of net deposition: hence the choice of CF^+ and CF_2^+ in this section, which results in net deposition on Si in the energy and angle of impact range we have studied here.

The transition between etching and deposition depends on the etch yield of the material impacting the surface and the underlying material. Steady state corresponds to a constant composition depth profile, after translating the origin with either the net etching or the deposition rate. Therefore, if steady-state etching is to occur, the underlying material will be mixed into the region near the surface with some of the incoming ion material. Steady state can be reached only if this mixing occurs. In contrast, under depositing

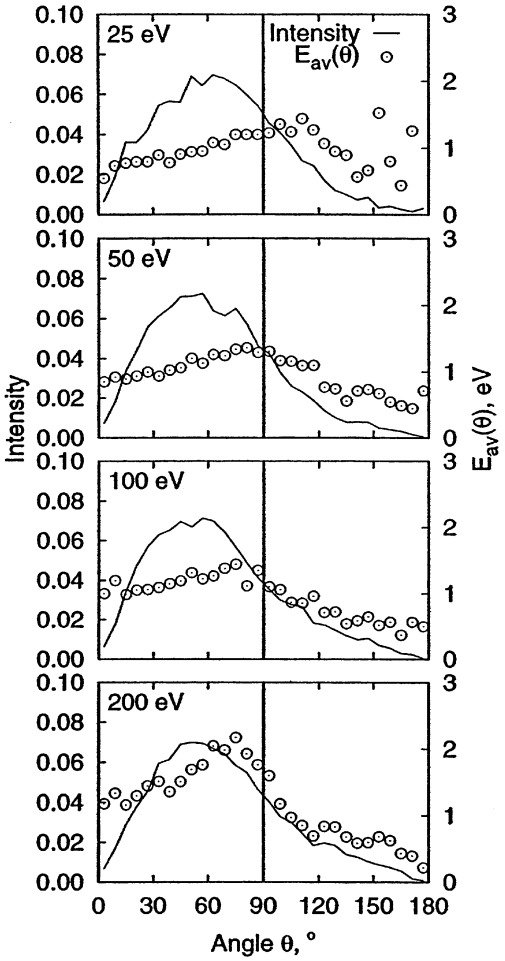

FIG. 30. Product angular distributions, with corresponding average kinetic energy as a function of angle, for E's of 50, 100, and 200 eV. Products for which $\Theta > 90°$ are "direct" and products for which $\Theta > 90°$ are "indirect." (From Abrams and Graves, 2000c.)

conditions, the material from the impacting ion cannot be removed faster than it deposits, and a film builds up. Of course, the composition of the film is not, in general, the same as the composition of the incoming ion. Some preferential sputtering of one component relative to another will generally occur.

In Fig. 31, the evolution of the composition of the surface as a function of ion fluence is shown for CF^+ impact (normal incidence) at 50, 100, and 200 eV. Note that the C and F content increases continuously, representing steady deposition. A small amount of Si is lost at the early stages for the

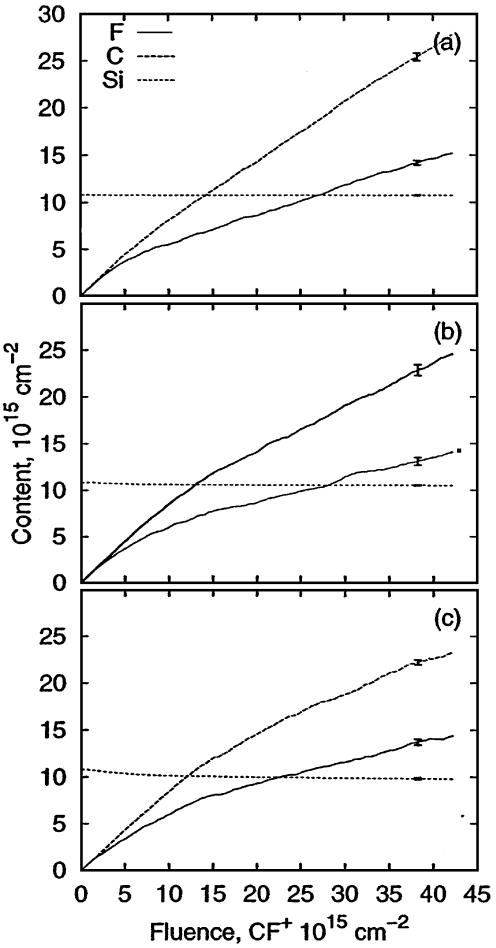

FIG. 31. Uptake of F and C as a function of fluence of CF^+ for E_i = (a) 50 eV, (b) 100 eV, and (c) 200 eV. Data shown are the average of three independent runs for each E_i, and error bars show standard deviations averaged over the fluence for each element content. (From Abrams and Graves, 2000a.)

higher energies. Note also that at the early stages of impact, the slopes of the lines are nearly unity, indicating near-unity sticking coefficients on bare Si. The slopes decrease until reaching a steady value. This occurs after about 5×10^{15} cm^{-2} fluence at 50 eV but not until about 15×10^{15} cm^{-2} at 200 eV. The corresponding plot for CF_2^+ is shown in Fig. 32. Note that after an initial period of deposition for these cases, the coverages (equivalently, surface content) of C and F appear to stop increasing significantly. CF_2^+ appears to result in a finite film thickness that stops increasing after it reaches a

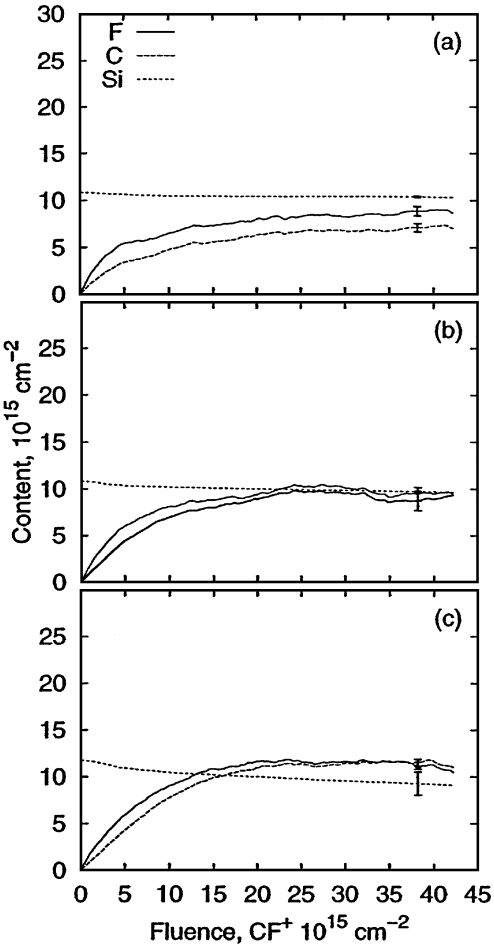

FIG. 32. Uptake of F and C as a function of the fluence of CF_2^+ for E_i = (a) 50 eV, (b) 100 eV, and (c) 200 eV. Data shown are the average of three independent runs for each E_i, and error bars show standard deviations averaged over the fluence for each element content. (From Abrams and Graves, 2000a.)

certain value. This is an example of a case in which the film reaches a certain thickness and stops growing. Of course, it needs to be kept in mind that given the approximate nature of the interatomic potentials, the behavior we observe in the simulations may or may not represent quantitatively what would be observed in the lab under the same conditions. However, tests of the sensitivity of the results to the choice of form of interatomic potential and to parameter values within a form of potential (Abrams, 2000) indicate that qualtitative results are trustworthy.

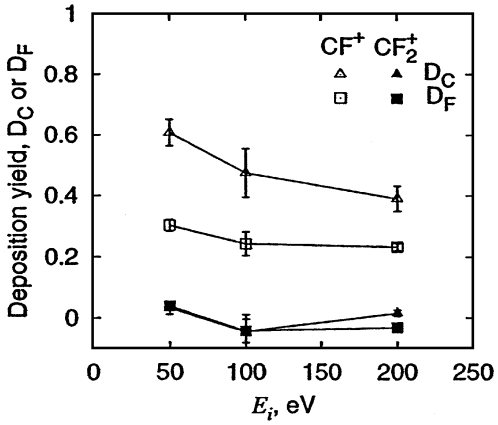

FIG. 33. Deposition yield of F and C vs E_i for both CF^+ and CF_2^+ ions. (From Abrams and Graves, 2000a.)

Figure 33 is a plot of the (steady-state) deposition yields of C and F for the two ions at 50, 100, and 200 eV. The deposition yield is defined as the slopes of the uptake curves in Figs. 31 and 32, that is, they are the net probability of deposition. The values near zero for CF_2^+ indicates that steady-state deposition probabilities are near zero. For CF^+, the ratio of C/F in the film stays near 2, but decreases slightly as energy increases. The sticking coefficients for these cases are plotted in Fig. 34. The sticking coefficients are defined in terms of the C and F in the impacting ions alone, ignoring

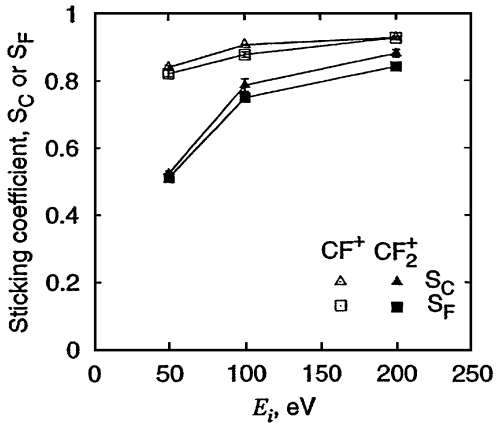

FIG. 34. Sticking coefficients of F and C vs E_i for both CF^+ and CF_2^+ ions. The magnitudes of the standard deviations for each data point are generally smaller than the symbol size. (From Abrams and Graves, 2000a.)

simultaneous removal of material already on the surface. The ion fragments more on impact at higher energy, and the fragments penetrate more deeply, resulting in a higher probability of sticking. The sticking coefficients for both C and F are above 0.8 for both ions at 200 eV.

The depth-resolved composition profiles as a function of the ion fluence for CF^+ at 100 eV are shown in Figs. 35a–d. Note that these profiles are the spatial analogues of the integrated content curves shown in Fig. 31. At a fluence of 2×10^{15} cm^{-2}, the C and F profiles are nearly identical, but by 10^{14} cm^{-2}, the C content is nearly twice the F content. From this point, it is clear that depositon will predominate, and to first order, the film simply grows

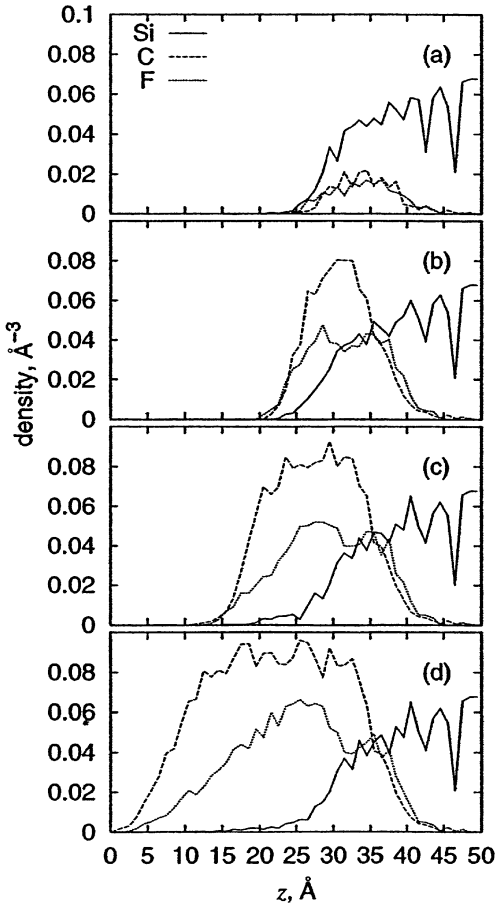

FIG. 35. Evolution of the C, F, and Si depth profiles for the surface layer grown by 100-eV CF^+ bombardment, at fluences of (a) 2.0, (b) 10.0, (c) 20.0, and (d) 40.0×10^{15} cm^{-2}. (From Abrams and Graves, 2000a.)

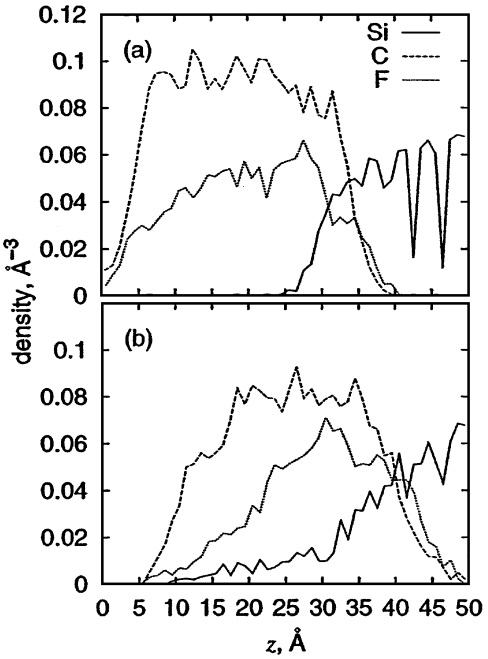

FIG. 36. C, F, and Si depth profiles for the surface layer grown by (a) 50-eV and (b) 200-eV CF^+ bombardment, at a fluence of 40×10^{15} cm^{-2}. (From Abrams and Graves, 2000a.)

at a constant composition with $C/F \sim 2$. Figures 36a and b are snapshots of the depth profiles after a fluence of 4×10^{14} cm^{-2} for 50- and 200-eV ions, respectively. The main point here is that the higher-energy ions have a lower deposition rate, and the Si has been more strongly mixed into the fluorocarbon layer. The C/F ratio is about 2 for both ion energies. Obviously, the film composition is not the same as the impacting ion: more C sticks than F, probably because F is attached to the surface with a single bond, whereas C can bond much more strongly. Finally, the approximate thickness of the layer in which C and Si overlap—the "interfacial thickness"—is plotted as a function of the ion energy for the two ions in Fig. 37. This value increases from about 6 to above 10 Å as the energy is increased from 50 to 200 eV.

The results of these simulations have shown that the transition from etching to deposition depends critically on the amount of F that remains in the film, especially in the first 1 or 2 ML of fluence. At 50 eV, the underlying Si is scarcely disturbed and the Si profile remains mostly unchanged, but at 200 eV, the Si mixes over 10–15 Å or more. These results have implications for ion-assisted film deposition and adhesion promotion and the character of the film–substrate interface. Also, in etch tools, it is very common to observe

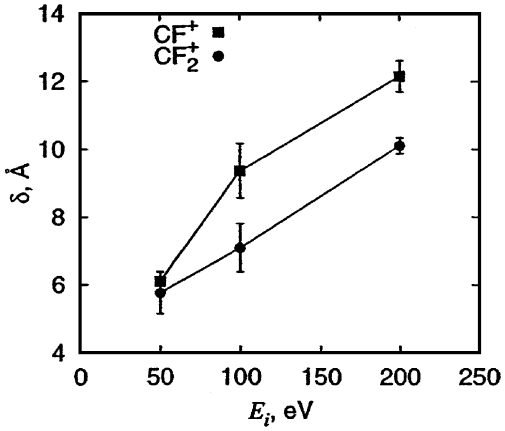

FIG. 37. Interfacial $Si_xC_yF_z$ layer thickness d at steady state vs E_i for CF^+ and CF_2^+ ions. The error bars show the standard deviation among the three runs averaged for each point. (From Abrams and Graves, 2000a.)

film deposition on walls and even on parts of the wafer surface while etching is occurring. Both tool-scale and feature-scale models require reasonably quantitative models of these processes, and the hope is that the atomic-scale insights provided by MD simulations will lead to reliable phenomenological models suitable for those purposes.

IV. Concluding Remarks

MD simulations of plasma–surface, especially ion– or fast neutral–surface interactions, have clearly generated considerable insight into some of the processes that are important in surface modification by plasmas. Equally apparent is that the work has only begun truly to understand and control plasma–surface processes. MD works very well for a few species interacting strongly over a few tens of angstroms and several picoseconds to perhaps a nanosecond. Even with these restrictions, only a handful of the many possible compounds have had many body potentials developed for this use. The potentials that have been applied are clearly approximations, and more work is needed to make them more quantitative. The role of charged species and excited states may be important in some cases, and this has been largely unexplored. Diffusion, reaction, and other processes that take place over time scales from microseconds to seconds under typical conditions need to be

incorporated into the simulation scheme, since room-temperature radicals and stable molecules are known to play important roles in surface modification. The focus in this article has been on etching, and deposition is treated elsewhere in this volume. There are other applications involving replacement or alteration of surface functional groups by plasmas that have not been studied to any significant extent using atomistic simulations.

It can be stated with confidence that developing improved control of atomic structure and configuration at surfaces over macroscopic length scales (such as a 300-mm-diameter wafer) will continue to increase in importance. Evolutionary improvements in electronic devices, photonic devices, and magnetic storage and display devices, among others, will continue to drive this need. Simulations of the processes that are used to manufacture such devices will likely become crucial aids to the interpretation of experiment and to the development of the associated manufacturing technology.

ACKNOWLEDGMENTS

The authors relied heavily on the work of Maria Barone and Bryan Helmer, and their many insights and contributions are gratefully acknowledged. Junichi Tanaka and Koji Satake contributed many insights as well, and we are grateful to them. The authors acknowledge support from the University of California SMART, Lam Research Corporation, National Science Foundation, and Semiconductor Research Corporation.

REFERENCES

Abrams, C. F., *Molecular Dynamics Simulations of Plasma-Surface Chemistry,* Ph.D. dissertation, University of California, Berkeley, 2000.

Abrams, C. F., and Graves, D. B., *J. Vac. Sci. Technol. A,* vol. 16, no. 5, pp. 3006–3019 (1998).

Abrams, C. F., and Graves, D. B., *J. Appl. Phys.* **86**(11), 5938–5948 (1999).

Abrams, C. F., and Graves, D. B., *J. Vac. Sci. Techol. A,* **in press** (2000a).

Abrams, C. F., and Graves, D. B., *J. Appl. Phys.* **88**(6), 3734–3738 (2000b).

Abrams, C. F., and Graves, D. B., *Thin Solid Films* **374**(2), 150–156 (2000c).

Abrams, C. F., and Graves, D. B., *J. Vac. Sci. Technol. A* **18**(2), 411–416 (2000d).

Allen, M. P., and Tildesley, D. J., "Computer Simulation of Liquids." Oxford University Press, New York, 1987.

Athavale, S. D., and Economou, D. J., *J. Vac. Sci. Technol. A* **13**(3), 966–971 (1995).

Barone, M. E., Atomistic Simulations of Plasma-Surface Interactions, Ph.D. dissertation, University of California, Berkeley, 1995.

Barone, M. E., and Graves, D. B., *J. Appl. Phys.* **77**(3), 1263–1274 (1995a).

Barone, M. E., and Graves, D. B., *J. Appl. Phys.* **78**(11), 6604–6615 (1995b).
Barone, M. E., and Graves, D. B., *Plasma Sources Sci. Technol.* **5,** 1–6 (1996).
Beardmore, K., and Smith, R., *Phil. Mag. A* **74**(6), 1439–1466 (1996).
Brenner, D. W., *Phys. Rev. B* **42**(15), 9458–9471 (1990).
Brenner, D. W., *Phys. Rev. B* **46**(3), 1948 (1992).
Chen, F. F., "Introduction to Plasma Physics and Controlled Fusion, 2nd ed." *Vol. 1. Plasma Physics,* Plenum Press, New York, 1984.
Coburn, J. W., and Winters, H. F., *J. Appl. Phys.* **50,** 3189 (1979).
Coburn, J. W., Winters, H. F., and Chuang, T. J., *J. Appl. Phys.* **48**(8), 3532–3540 (1977).
Coronell, D. G., Hanson, D. E., Voter, A. F., Liu, C.-L., Liu, X.-Y., and Kress, J. D., *Appl. Phys. Lett.* **73**(26), 3860–3862 (1998).
Feil, H., Dieleman, J., and Garrison, B. J., *J. Appl. Phys.* **74**(2), 1303–1309 (1993).
Galijatovic, A., Darcy, A., Acree, B., Fullbright, G., McCormac, R., Green, B., Krantzman, K. D., and Schoolcraft, T. A., *J. Phys. Chem.* **100,** 9471–9479 (1996).
Garrison, B. J., Reimann, C. T., Winograd, N., and Harrison Jr., D. E., *Phys. Rev. B* **36**(7), 3516–3521 (1987).
Haile, J. M., *Molecular Dynamics Simulation,* John Wiley and Sons, New York, 1992.
Hanson, D. E., Voter, A. F., and Kress, J. D., *J. Appl. Phys.* **82**(7), 3552–3559 (1997).
Hanson, D. E., Kress, J. D., and Voter, A. F., *J. Chem. Phys.* **110**(12), 5983–5988 (1998).
Harrison, D. E., *Crit. Rev. Solid State Mater. Sci.* **14**(Suppl. 1), S1 (1988).
Harrison, D. E. Jr., Levy, N. S., Johnson, J. P., and Effron, H. M., *J. Appl. Phys.* **39**(8), 3742–3761 (1968).
Harrison, D. E. Jr., Kelly, P. W., Garrison, B. J., and Winograd, N., *Surf. Sci.* **76,** 311–322 (1978).
Helmer, B. A., *Computer Simulations of Plasma-Surface Chemistry,* Ph.D. dissertation, University of California, Berkeley, 1998.
Helmer, B. A., and Graves, D. B., *J. Vac. Sci. Technol. A* **15,** 2252 (1997).
Helmer, B. A., and Graves, D. B., *J. Vac. Sci. Technol. A* **16**(6), 3502–3514 (1998).
Kress, J. D., Hanson, D. E., Voter, A. F., Liu, C. L., Liu, X.-Y., and Coronell, D. G., *J. Vac. Sci. Technol. A* **17**(5), 2819–2825 (1999).
Kubota, N. A., Economou, D. J., and Plimpton, S. J., *J. Appl. Phys.* **83**(8), 4055–4063 (1998).
Layadi, N., Donnelly, V. M., and Lee, J. T. C., *J. Appl. Phys.* **81,** 6738 (1997).
Lieberman, M. A., and Lichtenberg, A. J., *Principles of Plasma Discharges and Materials Processing,* John Wiley and Sons, 1994.
Oostra, D., Haring, A., de Vries, A., Sanders, F., and van Veen, G., *Nucl. Instrum. Methods Phys. Res.* **13,** 556 (1986).
Post, D. E., and Behrisch, R., (eds.), *Physics of Plasma-Wall Interactions in Controlled Fusion,* NATO ASI Series B, Plenum Press, New York, 1986.
Rapaport, D. C., *The Art of Molecular Dynamics Simulation,* Cambridge University Press, Cambridge, 1995.
Sigmund, P., *Phys. Rev.* **184**(2), 383–416 (1969).
Sikola, T., Armour, D. G., and den Berg, J. A. V., *J. Vac. Sci. Technol. A* **14,** 3156–3163 (1996).
Smith, R., Harrison, D. E. Jr., and Garrison, B. J., *Phys. Rev. B* **40**(1), 93–101 (1989).
Smith, R., Harrison, D. E. Jr., and Garrison, B. J., *Nucl. Instrum. Methods Phys. Res. B* **46,** 1–11 (1990).
Stillinger, F. H., and Weber, T. A., *Phys. Rev. Lett.* **62**(18), 2144–2147 (1989).
Tanaka, J., Abrams, C. F., and Graves, D. B., *J. Vac. Sci. Technol. A* **18**(3), 938–945 (2000).
Tersoff, J., *Phys. Rev. B* **38**(14), 9902–9905 (1988).
Tersoff, J., *Phys. Rev. B* **39**(8), 5566–5568 (1989).
Thompson, D. J., and Helms, C. R., *Surf. Sci.* **236,** 41–47 (1990).
Tully, J. C., *Annu. Rev. Phys. Chem.* **31,** 319–343 (1980).

Vyvoda, M. A., Abrams, C. F., and Graves, D. B., *IEEE Trans. Plas. Sci.* **27**(5), 1433–1440 (1999).
Vyvoda, M. A., *Surface Evolution during Integrated Circuit Processing,* Ph.D. thesis, University of California, Berkeley, 1999.
Winters, H. F., and Coburn, J. W., *Surf. Sci. Rep.* **14**(4–6), 161–269 (1992).
Wolf, S., and Tauber, R. N., *Silicon Processing for the VLSI Era, Vol. 1. Process Technology,* 2nd ed., Lattice Press, Sunset Beach, CA, 2000.